Journal of Structural Geology 161 (2022) 104659

Contents lists available at ScienceDirect

Journal of Structural Geology

journal homepage: www.elsevier.com/locate/jsg

Transtensional flanking structures

Franziska Mayrhofer [a], Martin P.J. Schöpfer [a,*], Marta Adamuszek [b], Marcin Dabrowski [b], Bernhard Grasemann [a]

[a] Department of Geology, University of Vienna, Austria
[b] Computational Geology Laboratory, Polish Geological Institute – National Research Institute, Wrocław, Poland

ARTICLE INFO

Keywords:
Flanking structures
Transtension
Structural glaciology
Pasterze

ABSTRACT

Flanking structures are deflections of an existing planar fabric (e.g., foliation) alongside a cross-cutting element (e.g., a vein) that can develop in a wide range of rock types and glacier ice. Nearly all published examples of flanking structures are interpreted to have formed either under simple shear or transpressional general shear, although theoretically they should also form under transtensional general shear. This paper describes the geometry and development of transtensional flanking structures in glacial ice of the Pasterze, Austria's largest alpine valley glacier. The cross-cutting elements are a few metres long and are interpreted as fractures that rotate into the shear flow and consequently accommodate anti- and synthetic offset, forming a- and s-type flanking folds. However, shear bands, with co-shearing cross-cutting elements inclined against the shear flow, are absent. The geometries of the mapped structures are successfully reproduced with a semi-analytical modified Eshelby solution for a frictionless cross-cutting element embedded in a linear viscous medium deforming under a remote transtensional sub-simple shear. The geometry of the mapped flanking folds, the absence of shear bands, the spatial variation of cross-cutting element orientations and the geometry of the glacier's splaying crevasses are consistent with two-dimensional transtensional sub-simple shear caused by down-glacier valley widening.

1. Introduction

Flanking structures (Passchier, 2001; Grasemann and Stüwe, 2001) are deflections of an existing planar fabric (e.g., foliation) alongside a cross-cutting element (CE; e.g., a vein) that can develop in a wide range of rock types, ranging from eclogites to unconsolidated sediments, and also glacier ice (e.g. Hamblin, 1965; Hudleston, 1989; Passchier et al., 2008). The classification scheme of flanking structures proposed by Grasemann et al. (2003) utilises the sense of drag and the offset of a central marker line along a CE with respect to the overall shear sense of the shear zone. On the basis of these parameters the family of flanking structures can be divided into extensional shear bands, contractional and extensional flanking folds with an antithetic offset (a-type) and contractional flanking folds with a synthetic offset (s-type), all of which can exhibit reverse or normal drag of the central marker. An alternative classification system for flanking structures, which is exclusively based on geometric criteria, was proposed by Coelho et al. (2005).

The instantaneous behaviour and progressive development of flanking structures in different rheologies around isolated and multiple, mechanically interacting CEs was elucidated by physical analogue, analytical and numerical models (Hudleston, 1989; Grasemann and Stüwe, 2001; Grasemann et al., 2003, 2019; Exner et al., 2004, 2006; Kocher and Mancktelow, 2006; Mulchrone, 2007; Fletcher, 2009; Exner and Dabrowski, 2010; Adamuszek and Dabrowski, 2017). However, all these studies focused on modelling of flanking structures under simple shear or transpressional general shear. An exception are the low-strain numerical models by Wiesmayr and Grasemann (2005), who suggested that transtensional flanking structures must also exist in nature. The main outcome of their modelling is that transtension promotes the development of a- and s-type flanking folds, but impedes the development of shear bands.

The present study describes transtensional flanking structures in glacier ice, which is practically speaking a monomineralic, metamorphic rock analogue that, in temperate glaciers, deforms at the pressure melting point. The rheological behaviour of ice is described by power-law creep (Glen's flow law; Glen, 1955), with an average power-law exponent of $n = 3$, although the dominant deformation mechanism depends on other factors, such as temperature, grain size, and strain rate. Analogies between structures in ice and rocks have been made by many authors (e.g., Hambrey, 1975, 1977; Hambrey and Milnes, 1975; Hooke

* Corresponding author.
E-mail address: martin.schoepfer@univie.ac.at (M.P.J. Schöpfer).

https://doi.org/10.1016/j.jsg.2022.104659
Received 24 December 2021; Received in revised form 10 June 2022; Accepted 14 June 2022
Available online 20 June 2022

and Hudleston, 1978; Kamb et al., 1985; Hudleston, 1989; Lawson et al., 1994), from the scale of a crystal (Wilson and Russell-Head, 1979; Montagnat et al., 2014) to tectonic systems (Sharp et al., 1988; Herbst and Neubauer, 2000). Comprehensive reviews of the discipline 'structural glaciology' are given by Hambrey and Lawson (2000), Hudleston (2015) and Jennings and Hambrey (2021).

Throughout this paper, transpressional and transtensional shear flow is, for the sake of simplicity, referred to as transpression and transtension, rather than narrowing and broadening sub-simple shearing, respectively (Simpson and De Paor, 1993), which also corresponds to type D plane strain transpression/transtension (Fossen and Tikoff, 1998). Clearly, plane strain deformation is an idealised concept that is rarely encountered in nature and triclinic flow (Lin et al., 1998) may result in complex progressive deformation, such as the formation of triclinic and/or highly non-cylindrical structures (e.g., Exner and Dabrowski, 2010; Adamuszek and Dabrowski, 2017). Nevertheless, the flanking structures in glacier ice described in the present study can, at least qualitatively, be reproduced via plane strain numerical modelling, and the spatial variation of the CE orientations can be explained by a plane strain kinematic model. More realistic modelling and analyses that acknowledge the three-dimensional nature and mechanics of glacier flow are beyond the scope of the present study.

2. Study area and methods

The Pasterze Glacier, with a length of 8.3 km, an area of 17.3 km^2 and a volume of 1.7 km^3 (in 2006; Lieb and Slupetzky, 2011), is the largest glacier in Austria and is located in the Penninic Tauern Window (Carinthia, Austria), just north of Austria's highest mountain, the Großglockner (3798 m a. s. l. UTM33, 324924E, 5216028N). The glacier can be divided into three areas (Fig. 1): (1) a wide accumulation area (Germ. Pasterzenboden, meaning "Pasterze's floor"), (2) a steep icefall (Germ. Hufeisenbruch, meaning "horseshoe-break", since in the past it was continuous and horseshoe-shaped) and (3) a gently sloping glacier tongue (the Pasterze *sensu stricto*). Since its last highstand of 1850 AD the Pasterze has been dramatically retreating (see Gspurning et al., 2004, and references therein) and in non-steady-state, with a response time of 34–50 years (Zuo and Oerlemans, 1997). The equilibrium line is currently above the top of the icefall. The orographic right part of the glacier tongue is covered with debris, resulting in lower ablation rates that hence affect the glacier's morphology (Kellerer-Pirklbauer et al., 2008). The recent glacier's recession is well documented on the basis of aerial surveys and photogrammetric mapping (Kaufmann et al., 2015).

Several structural glaciology studies were conducted on the Pasterze Glacier, such as the pioneering work on the foliation in glacier ice by Schwarzacher and Untersteiner (1953) and Untersteiner (1955), mapping of macroscopic structures (Herbst and Neubauer, 2000), structural interpretation from historic maps and aerial photographs (Herbst et al., 2006) and mapping of dominant structures from orthophotos and digital elevation models (Kellerer-Pirklbauer and Kulmer, 2019). These studies revealed that the glacier tongue comprises three flow units that form by confluence in the icefall; the orographic left unit is the widest and

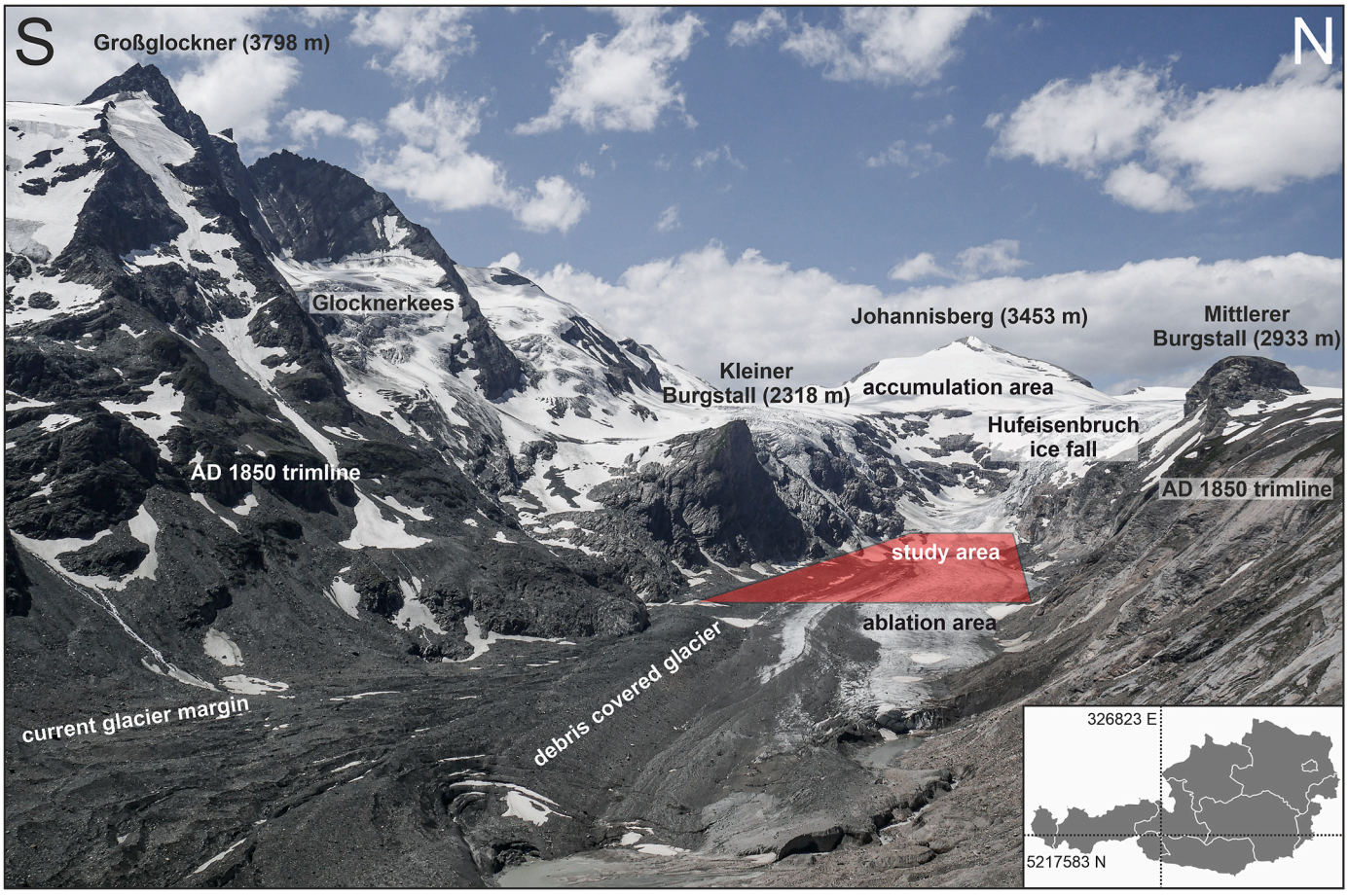

Fig. 1. The Pasterze glacier, north of the Großglockner, and its surrounding area, as viewed from the Kaiser-Franz-Josefs-Höhe (2369 m.a.s.l., UTM33 329246E, 5216017N). Selected geographic and glaciological features are labelled. The AD 1850 trim line marks the glacier's last highstand. The trim line is well-defined by vegetation on the northern valley side, but poorly developed on the southern side, which was covered by tributary glaciers, such as the 'Glocknerkees', that merged with the Pasterze (the 'Glocknerkees' lost its connection in 2009). The study area is located in the upper reaches of the glacier tongue. The inset shows Austria's political boundary, the federal states' boundaries and the location of the Pasterze glacier (Easting and Northing).

delineated from the central unit by a medial moraine, whereas the right unit is nowadays fully debris-covered (Fig. 2).

The present study focuses on mapping and analysing structures within a ca. 1.4 km long area located in the upper reaches of the glacier tongue which are not affected by collapse features, such as ice cauldrons forming by the collapse of ice overlying supraglacial meltwater channels (Figs. 1 and 2). In the summers of 2016–2020, mapping was carried out with the aid of high-resolution drone photogrammetry (see Appendix A for details) and the structures' orientations were measured using traditional field techniques. Annual position measurements of a stake network were utilized to determine mean annual velocities and strain rates (see Appendix B for details).

3. Structural assemblage

3.1. Morphology, velocities and strain rates

In the upper reaches of the study area, the glacier is ca. 300 m wide and its surface is relatively steep (ca. 15°), with an annual flow velocity of 27 m/a (see Table B1 for stake data). It widens down-glacier to a width of ca. 700 m and its surface becomes shallowly inclined (ca. 5°), with annual flow velocities gradually decreasing to about 5 m/a (Fig. 2). Maximum shortening rate orientations in the glacier's central region are parallel to the overall flow direction and their magnitudes decrease down-glacier from -1.5×10^{-9} s^{-1} (-0.05 a^{-1}) to about -2.5×10^{-10} s^{-1} (-0.008 a^{-1}). Lower marginal flow velocities lead, as expected, to maximum shortening rate orientations that are, in map view, typically inclined against the shear flow (Fig. 2); the two northernmost strain rates were computed from positions that form obtuse triangles with their long sides sub-parallel to the flow direction, possibly leading to maximum shortening rate orientations that are inconsistent with this general pattern. Although annual velocity directions and magnitudes and the maximum shortening rate orientations are generally consistent with the horizontal flow field of valley glaciers (e.g., Hooke, 2019), the sparse network of stakes does not permit a more detailed description. However, the structural assemblage provides further clues to the glacier's flow field.

3.2. Crevasses

Many crevasses along the glacier margin are due to collapse over subglacial streams. The majority of crevasses are however most likely due to fracture during glacial flow (Fig. 3a). In the upper reaches of the study area and a few 10s of metres further to the NW, transverse crevasses are present, most likely formed by the glacier's acceleration as it flows down the aforementioned incline. Another transverse crevasse field is located in the SE, close to the study area's lower end. The predominant set comprises splaying crevasses that clearly cut through the boundary between the left and central flow unit, suggesting similarity in rheological behaviour and a smoothly varying stress field between the left and central flow units. They form at an angle of ca. 30° to the boundary between the central and right flow unit and curve towards the glacier's centreline where they become parallel to the flow direction and hence longitudinal crevasses (Fig. 3a). This crevasse pattern is consistent with Nye's model that predicts this geometry in the presence of a longitudinal compressive stress (Nye, 1952; Hudleston, 2015; Jennings and Hambrey, 2021). Even though the stake network is sparse, the orientation of the splaying crevasses is consistent with the maximum shortening orientations (Fig. 2; see Harper et al., 1998, and references therein). A quantitative description and an alternative approach for predicting the splaying crevasses' curvature is given in Section 6. A minor crevasse set is orthogonal to the splaying crevasses, which could be referred to as 'cross-crevasses', analogous to orthogonal cross-joints in rock (e.g., Bai et al., 2002), although their origin in glacial ice is yet unexplained.

3.3. Foliation

The foliation is the most prominent fabric element in the study area and in the entire glacier tongue. Since the glacier enters the valley via the icefall, it is already foliated; it is doubtful that any traces of primary stratification (s_0) remain (Hudleston, 2015). The initial planar fabric formed by flow through the icefall is referred to as s_1. As the glacier flows down the aforementioned incline and decelerates in the shallower region, it forms folds with steeply plunging axes and steeply dipping axial planes striking transverse to flow (coined 'mushroom' folds by Ragan, 1969; see also Hambrey and Lawson, 2000). The folds are well developed in the central area of the left flow unit. The visibility of these folds however strongly depends on light conditions and view angle; they are best seen from the hiking trail "Gamsgrubenweg" along the NE side of the valley. These folds tighten due to continued longitudinal shortening and become dismembered as the new foliation s_2 forms further down-glacier. In both flow units, foliation s_2 dips inward and up-glacier, resembling geometrically "nested spoons" (Fig. 3b; Hambrey and Milnes, 1975; Herbst and Neubauer, 2000; Hudleston, 2015). Along the centreline of the left flow unit, the foliation dip decreases from >50° to as low as 20° down-glacier. The dip increases towards the left margin and at the boundary between the left and central flow unit foliation s_2 is sub-vertical.

3.4. Flanking structures

The vast majority of flanking structures are exposed in a ca. 1 km long and 50 m wide area along the right margin of the left flow unit (Figs. 2 and 3). This area is, due to transverse variations of the horizontal ice flow velocity, subjected to map-view dextral shearing. Later descriptions of CE orientations refer to this overall sense of shearing, e.g. a CE inclined against the shear flow has a map-view inclination of >90°, where the inclination angle is measured anticlockwise from the overall glacier flow direction. Quantitative comparison of digital elevation models in mid-July and mid-September 2020 revealed that the ablation in this strip is almost constant and about 5 m per two summer months. However, due to the nature of the flow field within the ablation area of a glacier (Hooke, 2019), flanking structures exposed at the down-glacier end of the mapped area must have formed at greater depth in the glacier than the structures exposed at the up-glacier end.

The CEs are up to a few metres long (average length 3.6 m; standard deviation 1.8 m) and are interpreted as open or closed fractures (e.g., moulins, crevasses, crevasse traces, veins) that rotate into the flow direction and consequently accommodate anti- and synthetic offset of the sub-vertical foliation, which serves as an excellent passive marker since the CEs' rotation axis is sub-vertical. The majority of isolated flanking structures can be classified as reverse drag a-type, normal drag s-type or reverse drag s-type flanking folds (Grasemann et al., 2003; Wiesmayr and Grasemann, 2005). Many of the observed flanking structures develop along mechanically interacting sets of CEs, resulting in complex and harder to interpret structures (Exner et al., 2006); these more complex structures are not described here.

One well-exposed example of a reverse drag a-type flanking fold, as seen when standing on the glacier, is shown in Fig. 4a. The CE dips steeply towards the NNW and the fold axes (of both, the up- and down-glacier flanking fold) plunge steeply towards the NNW. The π-axes (poles to the best-fit π-circles, fitted to poles of foliation) are consistent with the measured fold axes, supporting the field observation that the flanking folds are close-to cylindrical. Orientation data for all flanking structures measured in the field are shown in Fig. 4b, illustrating that the orientation of the CEs varies significantly, but systematically as discussed in Section 6.

A selection of representative flanking structures is shown in Fig. 5. The majority of the flanking structures' CEs are strongly localized shear zones, which developed on precursor discontinuities such as crevasses or veins. The shear zones have a thickness of 1–5 cm and frequently exhibit

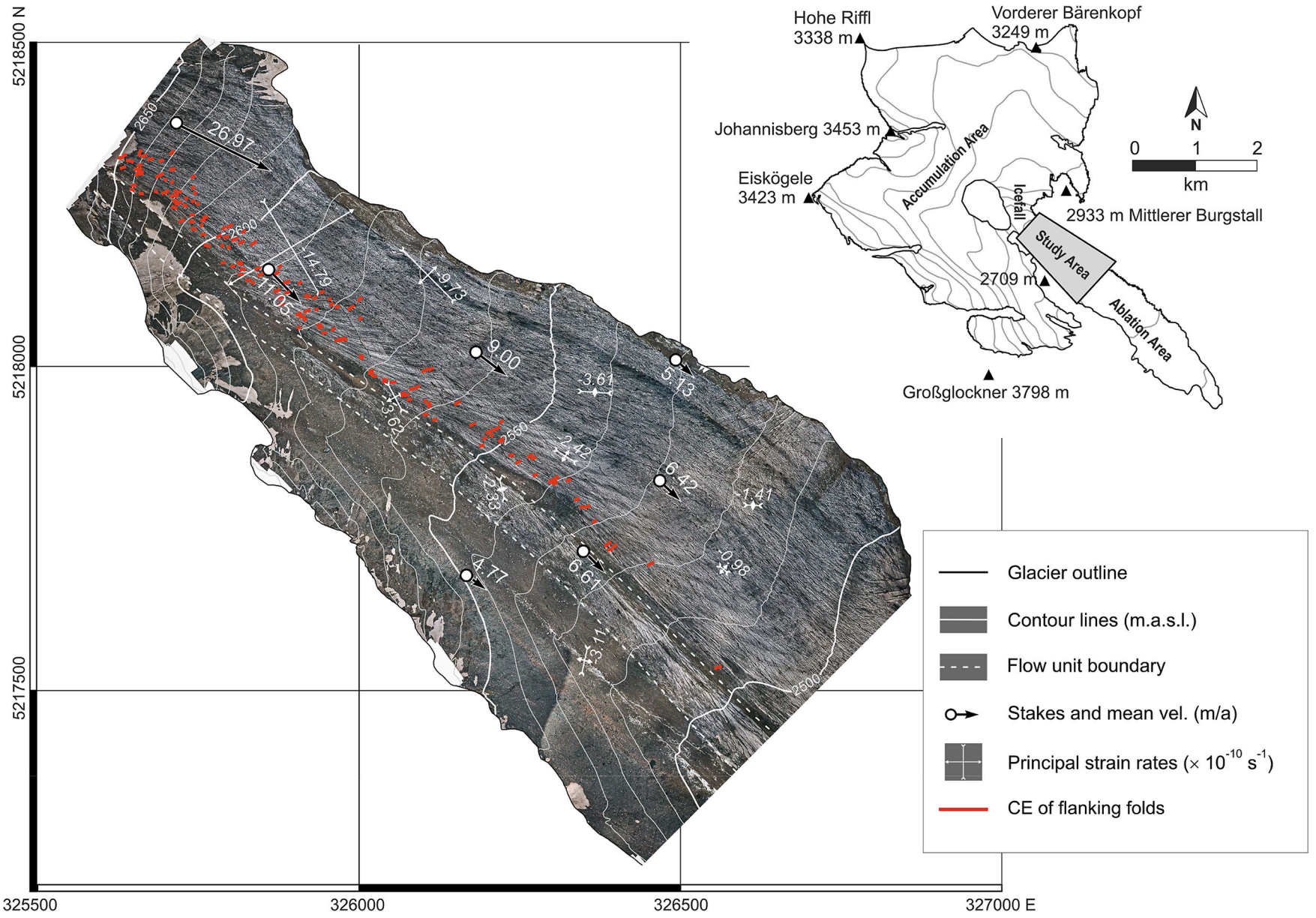

Fig. 2. Drone map of the study area from July 2020, with elevation contours (in m.a.s.l.), annual flow velocities (in m/a; arrows) and corresponding strain rates (italic numbers are maximum shortening rates $\times 10^{-10}$ s^{-1}). The traces of the cross-cutting elements (CEs) are also shown. The inset shows the outline of the entire glacier, selected mountain peaks and the map's location.

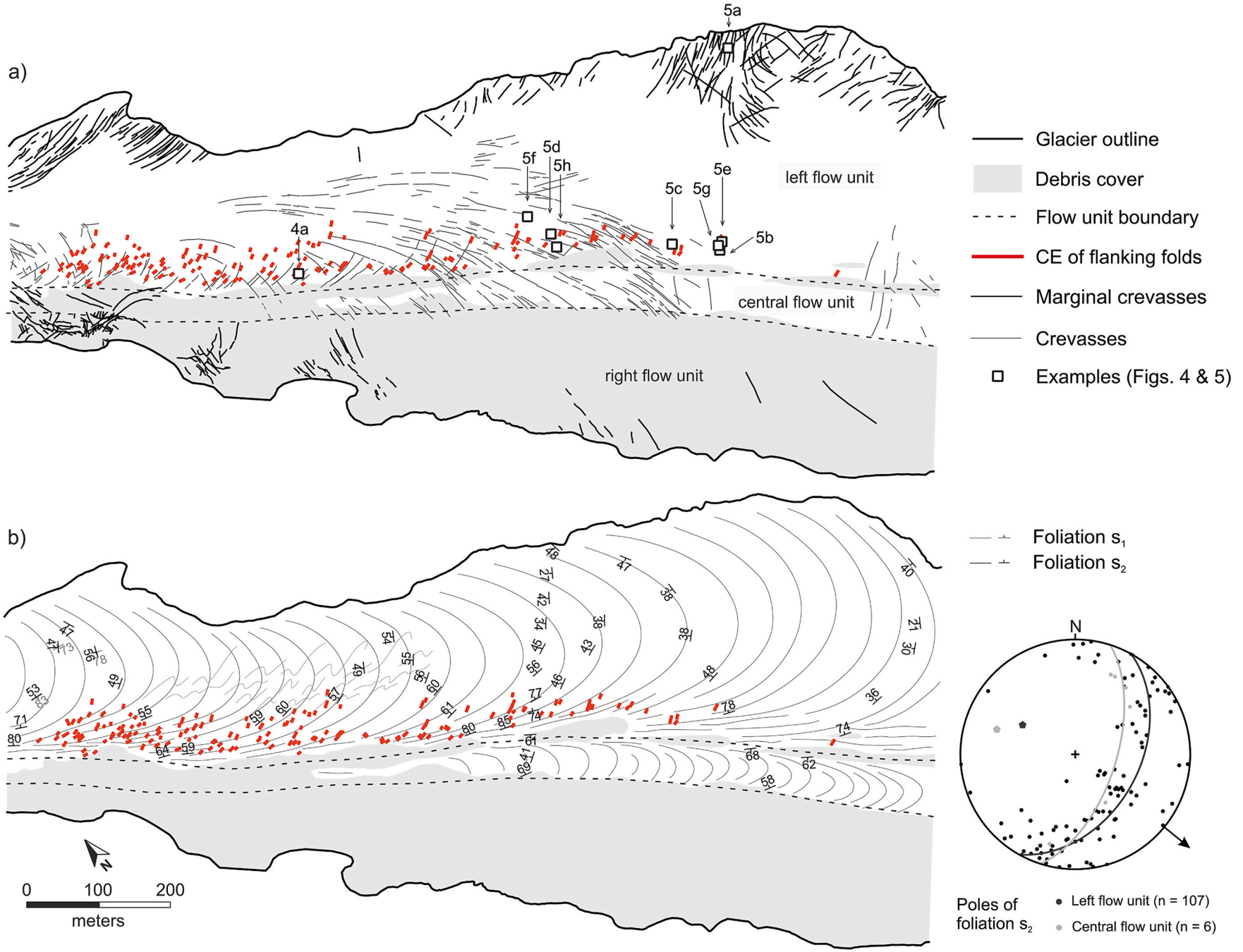

Fig. 3. Structural maps of the study area, based on two drone maps (July and September 2020), showing the glacier outline and its debris cover, together with the traces of the cross-cutting elements (CEs). (a) Map of interpreted crevasses. Labelled boxes indicate the locations of selected flanking structures shown in Figs. 4a and 5. (b) Map of interpreted foliation(s). The foliation orientation is given at selected location with strike and dip symbols (with dip angle). The stereoplot (equal area, lower hemisphere) shows orientation data taken during all field campaigns (2016–2020) of the foliation outside the flanking structures (together with best-fit great circles for the left and central flow unit). Arrow denotes approximate glacier flow direction.

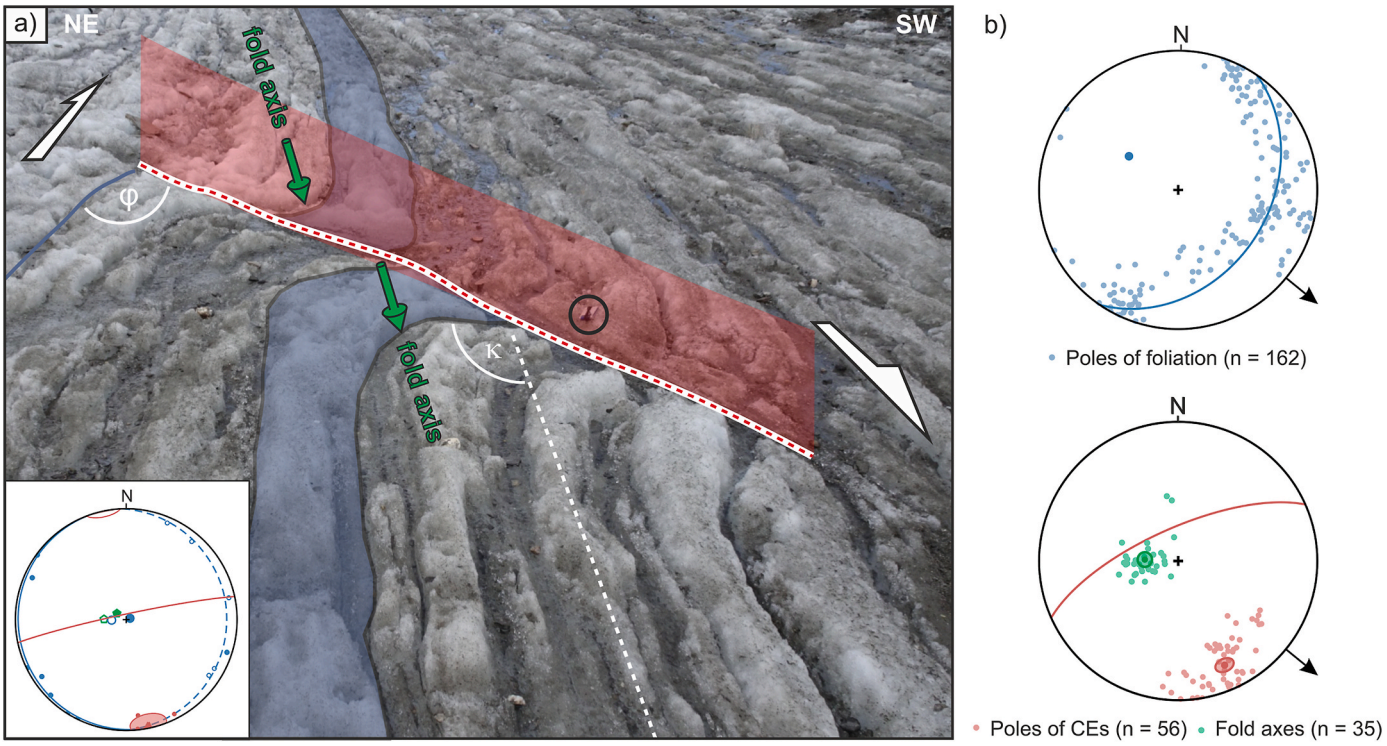

Fig. 4. (a) Example of a flanking structure as seen when standing on the glacier's surface, looking down-glacier (UTM33 - 5218143N, 325817E; see Fig. 3a for location). Compass (circled) for scale. Uninterpreted photo is provided as an electronic supplement. The 'central marker' is shaded in blue and the CE is shown as a red surface. The up- and down-glacier fold axes are also shown. The angle between the CE and the flow direction (φ) and the bulge of the central marker (κ) are indicated. A stereoplot with structural data from the flanking structure is shown in the inset: Red poles are from the CE, together with Fisher mean vector (triangle; small circle is the 95% confidence interval) and corresponding great circle. Fold axes and poles to foliation are plotted separately, with filled and open symbols for measurements taken up- and down-glacier of the CE, respectively. Best-fit great circles (π-circles) to poles of up- and down-glacier foliation are plotted as solid and dashed lines, respectively. The corresponding π-axes are plotted as slightly larger symbols and are very close to the measured fold axes, indicating that the flanking folds of that particular structure are close to cylindrical. (b) Structural data (foliation, fold axes and CEs) from all flanking structures measured in the field. Small circles are the 95% confidence interval around the Fisher mean vector. Arrows denote approximate glacier flow direction. (For interpretation of the references to colour in this figure legend, the reader is referred to the Web version of this article.)

a new internal foliation. Macroscopically, the ice in the shear zones (CEs) appears to be less translucent and has a smaller grainsize than in the surrounding ice. Although initial layering generated by syntaxial vein growth or snow infill could have existed in the precursor discontinuities, fracture closure and antithetic shearing that commences once a CE has rotated through the orientation of maximum instantaneous shear strain rate (see Section 4) would have dismembered these earlier fabrics. Occasionally, flanking structures develop around presumably initially sub-circular moulins, which developed into elliptical-shaped open CEs (Fig. 5a).

The most frequently observed flanking structures are a-type flanking folds with an antithetic offset of <2 m, a neutral roll (single curvature) and a bulge of the central marker line of $45° < \kappa < 140°$ (Fig. 5b–d). The angle between the flow direction and the CEs is typically $30° < \varphi < 80°$, with the general trend that structures with lower φ exhibit less offset and have a more pronounced bulge. Out of the 159 mapped flanking structures (Figs. 2 and 3), only three are inclined against the shear flow. Normal and reverse drag s-type flanking folds exhibit synthetic offset of <1 m, over-roll and bulge angles of $50° < \kappa < 140°$ (Fig. 5e–h). The angle between the flow direction and the CE is $20° < \varphi < 60°$. Many structures show a pronounced change of drag along the CE, with reverse drag around one tip and normal drag around the other tip (Fig. 5g and h). Correspondingly, the bulge of the normal drag increases from the centre to the tip of the CE. In case of the example shown in Fig. 5g, the bulge increases from $\kappa = 45°$ to $\kappa = 135°$. Interestingly, s-type flanking folds with $\varphi < 20°$ are not present. A thorough orientation analysis of the CEs is provided in Section 6, which is however preceded by theoretical considerations and numerical modelling of the development of transtensional flanking structures (Section 4 and 5, respectively).

3.5. Interim summary

The mapped area of the Pasterze glacier exhibits a morphology, flow field, and structure that are consistent with a near-surface transtensional flow regime, an interpretation that is supported by the following observations: (i) The glacier's velocity decreases downstream, as expected for an ablation area (the maximum velocity occurs just below the equilibrium line in valley glaciers; Hooke, 2019). However, in the case of the mapped area, the velocity additionally decreases due to both a decrease of the glacier bed's slope and to significant valley widening, i.e. the Pasterze widens from a width of 300 mto 700 m over a length of about 1.4 km (Fig. 2). As will be shown in Section 7.1, a widening channel flow leads to transtension. (ii) The splaying crevasses form at an angle of <45° at the margin between the central and the much slower flowing right flow unit. They also curve towards the glacier's centreline to become longitudinal crevasses (Fig. 3a). If these crevasses nucleate parallel to the greatest compressive stress orientation (a likely scenario), then their geometry is consistent with longitudinal compression, as first postulated by Nye (1952).

Importantly, the flanking structures (Fig. 5) exhibit geometries and orientations that are also consistent with transtensional flow, as demonstrated by a theoretical treatment on their instantaneous and finite deformation (Section 4 and 5, respectively).

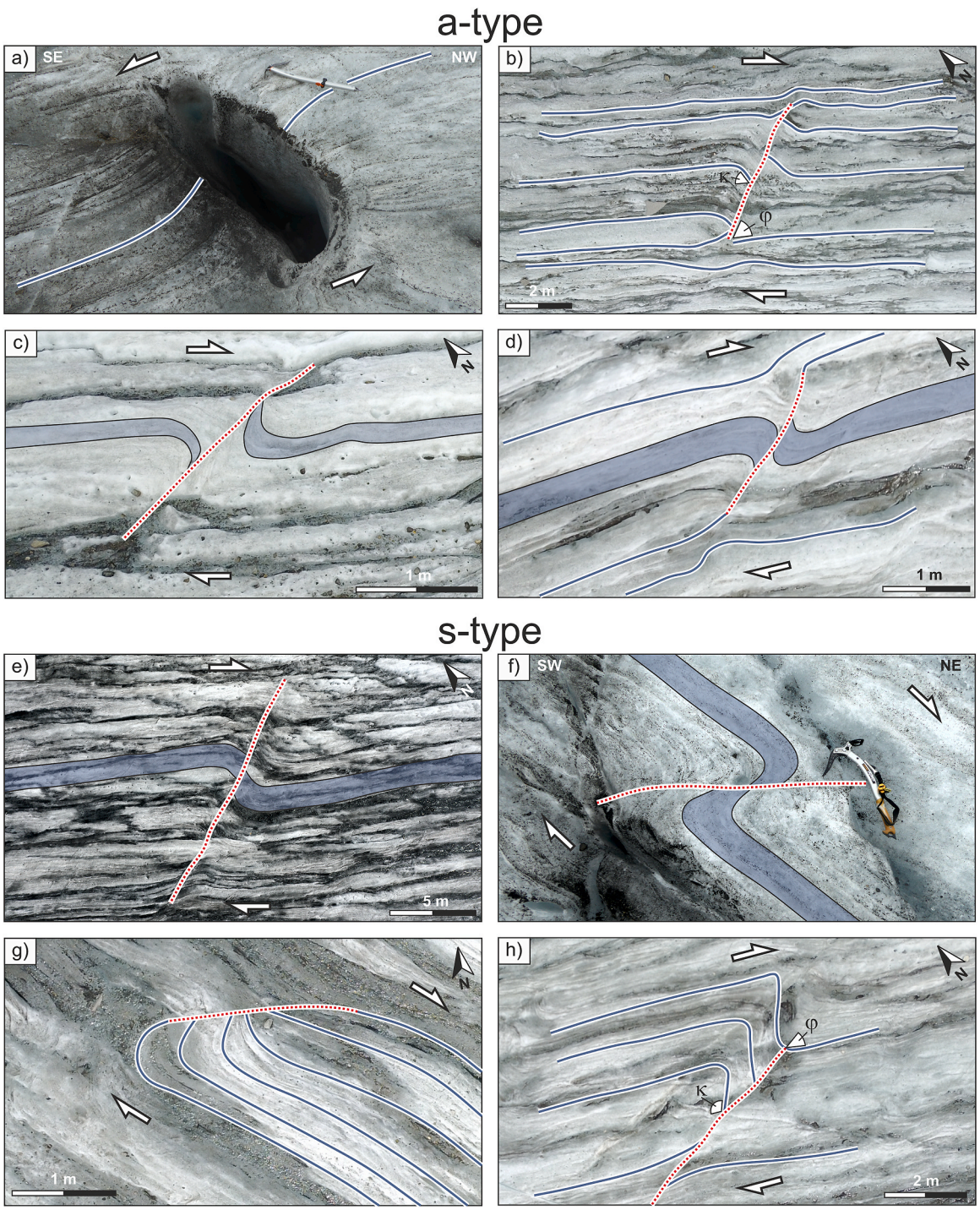

Fig. 5. Selected examples of a- and s-type flanking folds (see Fig. 3a for locations). The photos shown in (a) and (f) were taken with a hand-held camera (ice pick for scale), whereas all other photos were taken by a drone. Date of photo (d/m/y) and UTM coordinates are given below for each example. The angle between the CE and the flow direction (φ) and the bulge of the central marker (κ) are indicated in (b) and (h). Red dashed lines are CE traces and the markers (foliation) are traced in blue. (a) Presumably initially circular moulin deformed into an elliptical shaped CE, along which an a-type flanking fold developed (26/7/2016; 326653E, 5217918N). (b) a-type flanking fold ($\varphi \approx 60°$) with an antithetic offset of ca. 1 m, a neutral roll (single curvature) and a minimum bulge of $\kappa \approx 45°$ (13/7/2017; 326440E, 5217684N). (c) a-type flanking fold ($\varphi \approx 40°$) with an antithetic offset of ca. 80 cm, a neutral roll and a strong bulge of $\kappa \approx 45°$. (13/7/2017; 326389E, 5217739N). (d) a-type flanking fold ($\varphi \approx 40°$) with an antithetic offset of ca. 25 cm, over-roll and strong bulge of $\kappa \approx 115°$ (1/8/2017; 326254E, 5217873N). (e) s-type flanking fold ($\varphi \approx 60°$) with a synthetic offset of ca. 70 cm, an over-roll and a moderate bulge of $\kappa \approx 55°$ (16/7/2019; 326451E, 5217692N). (f) s-type flanking fold ($\varphi \approx 41°$) with a synthetic offset of ca. 20 cm, an over-roll and a strong bulge of $\kappa \approx 135°$ (26/7/2016, 326253E, 5217924N). (g) s-type flanking fold ($\varphi \approx 45°$), that exhibits a clear marker geometry only SE, i.e. down-glacier, of the CE, showing a transition from reverse to normal drag along the CE, with a bulge increasing from $\kappa \approx 45°$ to $\kappa \approx 135°$ (1/8/2017; 326443E, 5217691N). (h) s-type flanking fold ($\varphi \approx 35°$), that exhibits a clear marker geometry only around the CE's northern tip, showing a dramatic change from reverse to normal drag with a mean bulge of $\kappa \approx 105°$ (1/8/2017; 326245E, 5217854N). Uninterpreted photos are provided as an electronic supplement. (For interpretation of the references to colour in this figure legend, the reader is referred to the Web version of this article.)

4. Transpressional vs. transtensional flow fields

Progressive isochoric two-dimensional sub-simple shearing, loosely referred to in the present study as transpression/transtension if lengthening/shortening occurs parallel to the shear zone boundary, can be described with the following particle path equation (Ramberg, 1975)

$$\begin{bmatrix} x \\ y \end{bmatrix} = \begin{bmatrix} \exp(\dot{e}t) & (\dot{\gamma}/\dot{e})\sinh(\dot{e}t) \\ 0 & \exp(-\dot{e}t) \end{bmatrix} \begin{bmatrix} X \\ Y \end{bmatrix}, \tag{1}$$

where $\dot{e}$ is the elongation rate parallel to the shear zone boundary, $\dot{\gamma}$ a shearing rate and t the time; (X, Y) and (x, y) are the coordinates of a particle (components of position vectors) in the initial and deformed state, respectively. The ratio of shearing to elongation rate is related to the kinematic vorticity $W_k = \cos\alpha$ (Bobyarchick, 1986)

$$\dot{\gamma} / \dot{e} = -2\cot\alpha, \tag{2}$$

where α is the angle between the flow eigenvectors. Finite deformation resulting from progressive sub-simple shearing can be described, for a given finite stretch S parallel to the shear zone boundary, with the following position gradient tensor $\boldsymbol{F}$

$$\begin{bmatrix} x \\ y \end{bmatrix} = \begin{bmatrix} S & -\cot\alpha\left(S - S^{-1}\right) \\ 0 & S^{-1} \end{bmatrix} \begin{bmatrix} X \\ Y \end{bmatrix}. \tag{3}$$

Finite deformation of a unit square for dextral transpression and transtension are shown, for a shear zone parallel stretch $S = 1.2$ and its reciprocal, respectively, in Fig. 6. The component F_{12} of the position gradient tensor is 0.5 in both cases. The angle $\alpha = -\cot^{-1}[0.5/(S - S^{-1})]$ is hence negative/positive for transpression/transtension ($\alpha = \mp 36.3°$), whereas the kinematic vorticity is positive in both cases ($W_k = 0.81$).

The angle α can be constructed by means of a Mohr circle of the second kind (Simpson and De Paor, 1993). The circle is constructed by drawing a chord from the corner (F_{12}, F_{22}) to the point (F_{21}, F_{11}), where

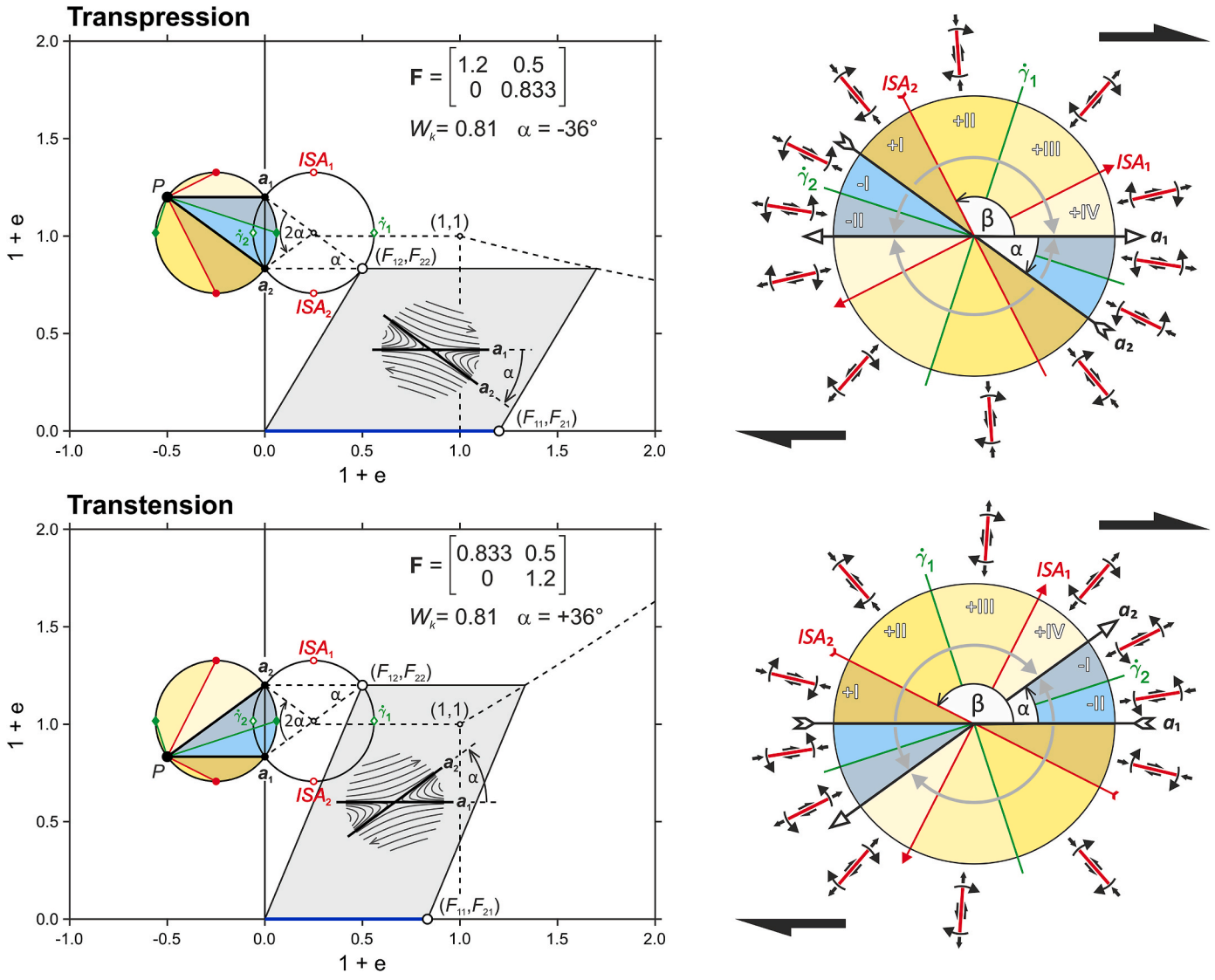

Fig. 6. Instantaneous behaviour (i.e. sense of slip, direction of rotation and elongation) for various orientations of a CE for isochoric plane strain transpression and transtension, illustrated by means of off-axis Mohr circle constructions and circular plots. The unfilled circles are Mohr circles of the second kind (Simpson and De Paor, 1993), which provide a direct link with physical space via the corner (F_{12}, F_{22}) of a deformed unit square (grey parallelograms). The filled circles are Mohr circles of the first kind (De Paor and Means, 1984), with pole P given by ($-F_{12}$, F_{11}), which can be used to construct various flow characteristic orientations in physical space. The dash-dotted line emanating from the corner (1,1) is a particle path for progressive transpression/transtension, drawn beyond the stage shown here (Eq. (1)). Streamlines are shown within a local coordinate system in the parallelogram centres. Note that the angle α is negative/positive under transpression/transtension, since it is measured clockwise/counter-clockwise in physical space from $\boldsymbol{a_1}$ to $\boldsymbol{a_2}$ (opposite sense within the Mohr circle of the second kind). See Section 4 for detailed description.

$F_{21} = 0$ in the present example; the length and midpoint of that chord is the circle's diameter and position, respectively (Fig. 6). In physical space, the angle between the chord and any shear zone parallel line (e.g., $y = F_{22}$) is the angle α, whereas in Mohr space, the central angle of the minor circular sector between points $(0, F_{11})$ and $(0, F_{22})$ is the double angle 2α. Although this Mohr circle construction provides a link with physical space (via the corner of a deformed unit square) and yields the correct angular relations (double angles), determining orientations via the pole method requires the construction of another circle by mirroring the existing circle across the ordinate (i.e., a Mohr circle of the first kind is constructed; De Paor and Means, 1984). The pole of this mirror image circle is $(-F_{12}, F_{11})$; chords emanating from this pole to any point on the mirror image circle provide the correct orientations in physical space. For clarity, the flow characteristic orientations, which are fixed for a given constant flow type with respect to the shear zone boundary, are shown in physical space as circular plots (Fig. 6). Additionally, the instantaneous sense of slip, direction of rotation and elongation of a hypothetical planar slip-surface, e.g. a CE in the present context, are shown.

The circular plots illustrate that six fields (labelled with roman capital numerals –II to IV) with different instantaneous behaviour of a CE can be discriminated. The eigenvectors $\boldsymbol{a_1}$ and $\boldsymbol{a_2}$ separate fields in which the CE is either co- or counter-rotating towards a stable orientation that is parallel to the divergent flow apophysis (Fossen et al., 1994), here simply referred to as 'fabric attractor' (Passchier 1997). Note that the terms co- and counter-rotating are used with respect to the overall sense of imposed shear, e.g. a co-rotating line rotates clockwise under dextral (clockwise) shear, and shall not be confused with clockwise and counter-clockwise (which depends on the view point). The two mutually orthogonal instantaneous stretching axes, ISA_1 and ISA_2, divide all possible orientations of the CE into two sectors with syn- and antithetic kinematics. The two mutually orthogonal maximum shearing orientations $\dot{\gamma}_1$ and $\dot{\gamma}_2$ are at 45° to the ISA_1 and ISA_2 orientations and separate fields in which the CE is either lengthening or shortening. Co-rotating (indicated by yellowish fields in Fig. 6) CEs can either experience synthetic slip/shortening (+I), antithetic slip/shortening (+II), antithetic slip/lengthening (+III), or synthetic slip/lengthening (+IV). Counter-rotating (indicated by blueish fields) CEs can only experience synthetic slip and are either shortening (-I) or lengthening (-II). Since W_k is identical for transpression and transtension (Fig. 6), the various flow characteristic orientations in physical space (i.e., the circular plots) under transtension are readily obtained by counter-rotating the orientations for transpression by the angle α.

Although the flow characteristic orientations and the instantaneous behaviour of a CE share many similarities in transpression and transtension, a fundamental difference is evident. The first flow eigenvector $\boldsymbol{a_1}$ is parallel to the shear zone boundary in both cases, but its eigenvalue is positive (lengthening) under transpression and negative (shortening) under transtension (note blue line at the base of the deformed unit square in Fig. 6). However, under isochoric two-dimensional sub-simple shearing, the eigenvector with a positive (lengthening) value is the fabric attractor (see also streamlines in Fig. 6). Consequently, the fabric attractor is under transtension not parallel to the shear zone boundary, a detail that has important implications for the progressive development of flanking structures.

During progressive deformation, a CE can rotate through the different fields depicted in Fig. 6 and hence its kinematics can change, for example, from syn-to antithetic and back to synthetic (Grasemann et al., 2019). Under transpression, the CE either co- or counter-rotates into the orientation of the shear zone-parallel fabric attractor, leading after large strain to s-type flanking folds or shear bands (Wiesmayr and Grasemann, 2005). In both cases, both the deflected marker lines and the CE become, after some shear strain, parallel to the shear zone boundary and the structures are dismembered (Grasemann et al., 2019). Under transtension, however, the fabric attractor is oblique to the shear zone boundary and, as shown by the numerical models described in Section 5, the CE co- or counter-rotates into this orientation, accumulating the synthetically offset marker lines at the CE's tips. Large strain always results in the formation of s-type flanking folds and shear bands are unstable. Under both transpression and transtension, a-type flanking folds are transient structures. The dominant presence of s-type flanking folds and the absence of shear bands may hence be indicative for high-strain transtensional shear zones.

It is important to note that the above account on the theoretical development and geometry of flanking structures assumes an initial planar fabric that is parallel to the shear zone boundary, which is parallel to the *x*-direction, or, the first flow eigenvector $\boldsymbol{a_1}$ (Fig. 6). If the initial planar fabric would be parallel to the fabric attractor under transtension, i.e. inclined by the angle α, then the resulting structures would be identical to those formed under transpression, since the flow invariants (and hence Mohr circle positions and radii) are identical.

5. Numerical modelling of transtensional flanking structures

5.1. Numerical models

The finite deformation resulting from progressive transtension around a CE that deforms homogeneously by stretching, rotation and shearing was modelled using an Eshelby solution, modified for viscous fluid modelling (Exner and Dabrowski, 2010); implementation details are provided in Appendix C. A series of models was run for a homogeneous transtensional background flow with five different kinematic vorticities $W_k = \{0.87, 0.77, 0.71, 0.64, 0.5\}$, corresponding to $\alpha = \{30°, 40°, 45°, 50°, 60°\}$, and three different initial CE orientations $\varphi_0 = \{50°, 90°, 130°\}$, where the angle φ_0 is measured counter-clockwise from the first flow eigenvector $\boldsymbol{a_1}$, as defined in Fig. 6 (the CE with $\varphi_0 = 130°$, for example, is initially inclined against the overall shear flow). Model results are shown for an initial planar fabric that is parallel to $\boldsymbol{a_1}$ and a finite effective shear strain $\gamma = 2$ in Fig. 7. Interestingly, the final geometry is not very sensitive to the W_k of the imposed deformation, but strongly dependent on φ_0. However, the reader should bear in mind that geometrical differences for a given W_k arise from the choice of both the CE and the initial fabric orientation relative to the fabric attractor of the imposed deformation. In the following, the terms 'overall shear' or 'shear flow' refer to the shearing parallel to the initial fabric.

In the $\varphi_0 = 50°$ models (first column in Fig. 7), the CE is initially inclined into the overall shear and its initial orientation is already close to the fabric attractor, which is under transtension parallel to the second flow eigenvector $\boldsymbol{a_2}$ (Fig. 6). In the $\alpha < 50°$ models, the CE rotates into the shear flow, in the $\alpha = 50°$ model the CE is initially already in a stable position (and hence only lengthens and accumulates displacement without rotating), and in the $\alpha > 50°$ model the CE rotates against the overall shear. Nevertheless, despite this different rotational behaviour of the CE, the finite flanking structure of these five models is very similar, even though the stable orientation of the CE varies: The central marker layer has a neutral roll and a negative bulge in the range $-40° < \kappa < -20°$. The strong reverse drag of the marker lines is compensated by folds developing at the CE's tips. The structures of the $\varphi_0 = 50°$ models can hence be classified as reverse drag s-type flanking folds.

In the $\varphi_0 = 90°$ models (second column in Fig. 7), the CE is initially normal to the overall shear and experiences instantaneous lengthening and rotation into the shear flow. Initially the sense of slip on the CE is antithetic, but reverses to synthetic once the CE has rotated through the orientation of the maximum instantaneous stretching axis (ISA_1; as illustrated in Fig. 6). Thus, an initial a-type flanking fold develops into a s-type structure. In all models, the central marker layer exhibits an overroll, a normal drag and a minor bulge in the range $25° < \kappa < 35°$. Clearly, in the higher kinematic vorticity models, the CE has not yet reached a stable orientation (parallelism with the fabric attractor). In the $\alpha = 30°$ model, the angle between the CE and fabric attractor is ca. 13°, whereas in the $\alpha = 60°$ model, it is ca. 5°. Nevertheless, more deformation would simply result in further rotation of the CE into the attractor and

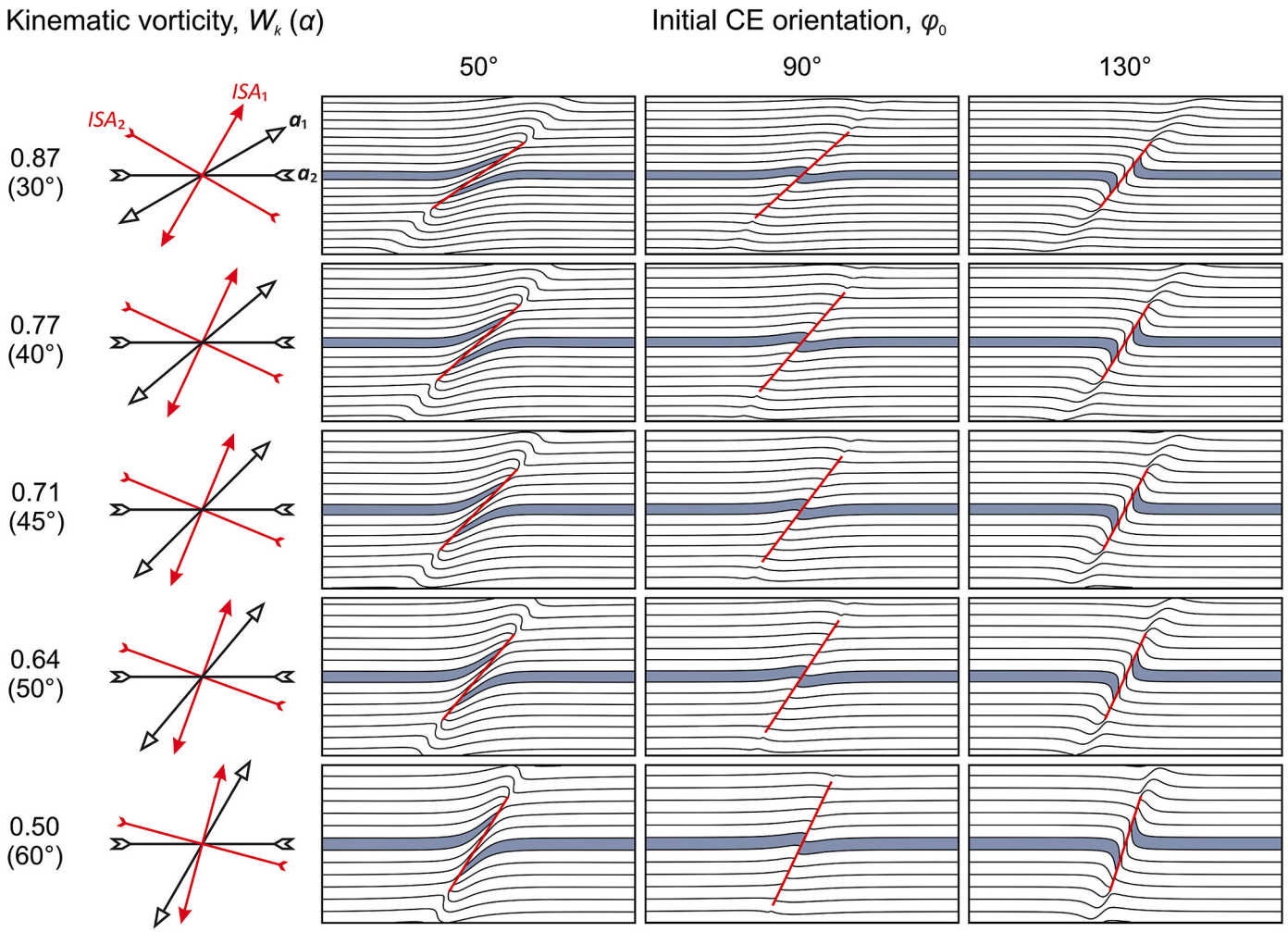

Fig. 7. Numerical modelling results of flanking structures formed under a homogeneous transtensional background flow with five different kinematic vorticities (W_k) and three different initial CE orientations (φ_0) after an effective shear strain of $\gamma = 2$. For each value of W_k, the (fixed) orientations of the eigenvectors of the flow ($\boldsymbol{a_1}$ and $\boldsymbol{a_2}$) and principal instantaneous stretching axes (ISA_1 and ISA_2) are shown. See Section 5.1 and Appendix C for details. Animations of all models are provided as an electronic supplement.

accumulation of additional synthetic displacement.

In the $\varphi_0 = 130°$ models (third column in Fig. 7), the CE is initially inclined against the shear flow and in all models the CE has not yet reached a stable position (in fact, the CEs are sub-parallel to the orientation of ISA_1). The CEs experience instantaneous shortening followed by instantaneous lengthening while rotating into the shear flow. The central marker layer exhibits antithetic shear with an extensional offset, reverse drag and a bulge of $\kappa \approx 90°$. The reversely dragged marker layers in the centre of the flanking structure exhibit a neutral roll, thin towards the CE and only in close vicinity of the CE's tips is the reverse drag compensated by normal drag. The structures of the $\varphi_0 = 130°$ models could be classified as a-type flanking folds, but note that further deformation of the CE and rotation towards the fabric attractor would occur in the field of synthetic slip, subsequently transforming the structure into an s-type flanking fold.

5.2. Comparison with natural flanking structures

The natural flanking structures (Fig. 5) share many similarities with the modelled structures (Fig. 7) and exhibit features that are in fact diagnostic for transtension: (1) Although the natural and modelled a-type flanking folds (Fig. 5a–d and third column in Fig. 7, respectively) are similar to previously modelled and natural structures that formed under transpression (e.g. Grasemann et al., 2003; Kocher and Mancktelow, 2005), transpressional shear zones frequently also include shear bands (Wiesmayr and Grasemann, 2005). However, the mapped area of the Pasterze glacier does not contain a single shear band, suggesting that shear bands are not stable in transtension. In summary, a-type flanking folds can form both in transpression and transtension and are hence not diagnostic features, but the co-existence of a-type flanking folds with shear bands is diagnostic for transpression. (2) Under transpression, s-type flanking structures can only form around CEs which are inclined into the overall shear flow with an angle of $\varphi < 45°$. In contrast, under transtension, s-type flanking fold can form around CEs with inclinations $\varphi > 45°$ (see for example models with $\varphi_0 = 50°$ or $\varphi_0 = 90°$ and $W_k = 0.5$ in Fig. 7 and natural example in Fig. 5e). (3) Flanking structures forming under transtension with an initial CE orientation φ_0 that lies between ISA_1 and the first flow eigenvector $\boldsymbol{a_1}$ (sectors –II, –I and +IV in Fig. 6) exhibit reverse drag of the central marker line (first column in Fig. 7). This pronounced reverse drag transitions into normal drag towards the CE's tips, forming folds (Fig. 5g and h) that accommodate the displacement on the CE. Once in a stable orientation, the CE continues accumulating displacement *ad infinitum*, although eventually the structure will fade into a new foliation, parallel to the fabric attractor. Such an s-type flanking fold, with central reverse drag that transitions towards the tips into normal drag and folding, is not observed forming under transpression (e.g., Grasemann et al., 2003).

6. Analysis and interpretation of orientation data

In this section the orientations of the CE traces, as interpreted on the drone map (red lines in Figs. 2 and 3), are analysed. The CEs ($N = 159$), with their lengths exaggerated by a factor five, and the glacier's annual mean velocities are plotted in Fig. 8a. Close inspection of that map reveals that the CEs are, in map view, inclined into the overall shear and that their orientation relative to the flow direction (φ) exhibits a systematic spatial variation. Specifically, φ increases from the SW to the NE, from the right margin of the left flow unit towards the glacier's centreline, where in the present context 'centreline' refers to the centre of the left flow unit where the flow velocity magnitude is maximum as indicated by the pattern of the s_2 foliation and not to the geographic centre of the glacier. A reference line was objectively chosen by letting the line pass through the mean position of all CEs and systematically varying its orientation until the maximum correlation coefficient between φ (angle between CE and reference line, measured counter-clockwise from the down-glacier direction; see inset in Fig. 8a) and the reference line's normal direction is attained (this optimised correlation is plotted in Fig. 8c). This optimised reference line is in fact sub-parallel to the average flow directions (Fig. 8a).

The CE inclinations (φ) are plotted vs. down-glacier distance (x) in Fig. 8b. Out of the 159 interpreted CEs, only three are inclined against the flow direction ($\varphi > 90°$); these are excluded in later analysis since they cannot have reached a stable orientation within a transtensional background flow. One isolated CE close to the study area's lower end is also excluded. The variability of the CE inclinations clearly decreases down-glacier, but there is no (significant) correlation between inclination and down-glacier distance. Nevertheless, when the CE inclinations SW and NE of the reference line are plotted separately (white and black circle in Fig. 8b, respectively), it is clear that the former have lower inclinations (arithmetic mean $\overline{\varphi} = 47°$) than the latter ($\overline{\varphi} = 65°$).

The CE inclinations (φ) vs. distance to the reference line (y) are plotted in Fig. 8c, together with the best-fit linear regression model (the function $\varphi(y)$ is given), the 95% confidence belt around the data and the regression. Even though the correlation is highly significant (p-value $= 7.72 \times 10^{-18}$), the data display some scatter, which is attributed to two potential sources: (1) Many CEs are interacting with each other, leading to complex structures that, as stated earlier, are not discussed here. Mechanical interaction can lead to orientations that are not parallel to the fabric attractor (Exner et al., 2006). (2) Some CEs may not have reached a stable orientation, in particular those located in the upper reaches of the zone (Fig. 8b). Nevertheless, in the subsequent analysis it is assumed that, on average, the CEs have reached a stable orientation, an assumption that is not far-fetched as discussed in Section 7.2.

If one assumes that the best-fit linear relation of φ vs. normal distance y provides the angle between the flow direction and the fabric attractor (α) it is possible to determine the vorticity ($W_k = \cos\alpha$) and the inclination of greatest shortening rate (ISA_2), which can be easily derived, either from the Mohr circle or from the circular plot shown in Fig. 6, i.e. $\beta = (\alpha + 270°)/2$. These relations are plotted in Fig. 8d within their theoretical bounds, i.e. from simple shear ($W_k = 1$) to pure shear ($W_k = 0$).

The (linear) function $\beta(y)$ should, in theory, provide an upper bound for the angle δ, measured between crevasses and the reference line (again, measured counter-clockwise from the flow direction), if one assumes that crevasses nucleate parallel to ISA_2, a likely scenario for the splaying crevasses. An upper bound is expected because once formed, the crevasses commence to co-rotate, i.e. their inclination δ will decrease during subsequent deformation. The map view inclinations of all traced crevasses are plotted vs. normal distance to reference line in Fig. 8e, together with the aforementioned theoretical upper-bound, which yields a good estimate for the maximum crevasse inclination. The normal distance from the reference line where pure shear conditions are expected ($\delta = 180°$) is also indicated in Fig. 8e (vertical dash-dotted line). A line drawn in map view which is parallel to the reference line and at this 'pure shear conditions' distance (dash-dotted line in Fig. 8f) is consistent with the approximate region where the splaying crevasses become longitudinal crevasses.

The aforementioned analysis is effectively one-dimensional since all orientations are analysed normal to the reference line irrespective of their down-glacier distance. Nevertheless, it is tempting to construct two-dimensional trajectories to illustrate how well the estimate of the ISA_2 orientation from the (assumed to be stable) CE orientations fits the map view geometry of the splaying crevasses. Since the inclination of ISA_2 is given by a linear function of the form $\delta = py + q$, the trace of a trajectory is readily obtained by integration

$$x(y) = \int \cot(py+q)dy = \frac{\ln[\sin(py+q)]}{p} + C \tag{4}$$

where C is the integration constant (e.g., when $C = \ln[\sin(q)]/p$ the trajectory passes through the origin). Trajectories for both $\boldsymbol{a_1}$ and ISA_2 are plotted in the local x-y-coordinate system in the inset in Fig. 8d. An ISA_2 trajectory, rotated to the global coordinate system, is also plotted onto a map of all crevasses in Fig. 8f, illustrating that the estimated upper bound for the crevasse orientations matches the splaying crevasses' geometry.

7. Discussion

7.1. Origin of transtension

As already summarised in Section 3.5, the glacier's morphology and its structural assemblage in the mapped area are consistent with a 'compressive flow' (Nye, 1952). This term is entrenched in the literature, although 'decelerating flow', and its counterpart 'accelerating flow', may be more descriptive. For a glacier in a gently undulating, parallel-sided valley, the conditions for the occurrence of longitudinal compression are (Nye, 1952):

$$\frac{dq}{dx} + \frac{q}{R}\cot\alpha < 0, \tag{5}$$

where x is the down-glacier direction, q is the discharge, i.e. volume passing through any cross-section in unit time, R is the radius of curvature of the bed and α is here the slope of the glacier's surface. For a uniformly sloping glacier bed ($R = \infty$), compressive flow is hence expected in the ablation area ($dq/dx < 0$). In the absence of accumulation or ablation ($dq/dx = 0$), a concave-up bed ($R < 1$) will lead to compression; additionally, down-glacier valley widening could lead to compression (it is enigmatic why Nye (1952), on p. 91, states the opposite). In the mapped area, all three factors are present, (i) ablation, (ii) shallowing of the glacier bed and (iii) valley widening. The theoretical velocity distribution and the slip-line field in a longitudinal section of an ideal valley glaciers on an undulating bed (Nye, 1951) and the theoretical crevasse patterns within an 'extending' and 'compressive' flow in a parallel-sided valley (Nye, 1952) are amongst the best-known diagrams in glaciology and shall hence not be further discussed here. However, even though Nye's model is consistent with the observed splaying crevasse geometries, it is inconsistent with the progressive transtensional deformation recorded by the flanking structures, which requires transverse extension that is not possible in a parallel-sided valley.

Nevertheless, valley widening also leads to a compressive flow and in fact transtension; this case is discussed here for a glacier of constant unit discharge and unit thickness (plane strain). Although solutions exist for diverging or converging channel flow (so-called Jeffery-Hamel flow), an analytical treatment is beyond the scope of the present study. Thus, a kinematic model that qualitatively encompasses the superficial velocity distribution of a glacier shall suffice (see Appendix D for details). The chosen velocity field (Fig. 9a) is a superposition of a uniform distribution, which accounts for slip at the channel margin, and a quadratic

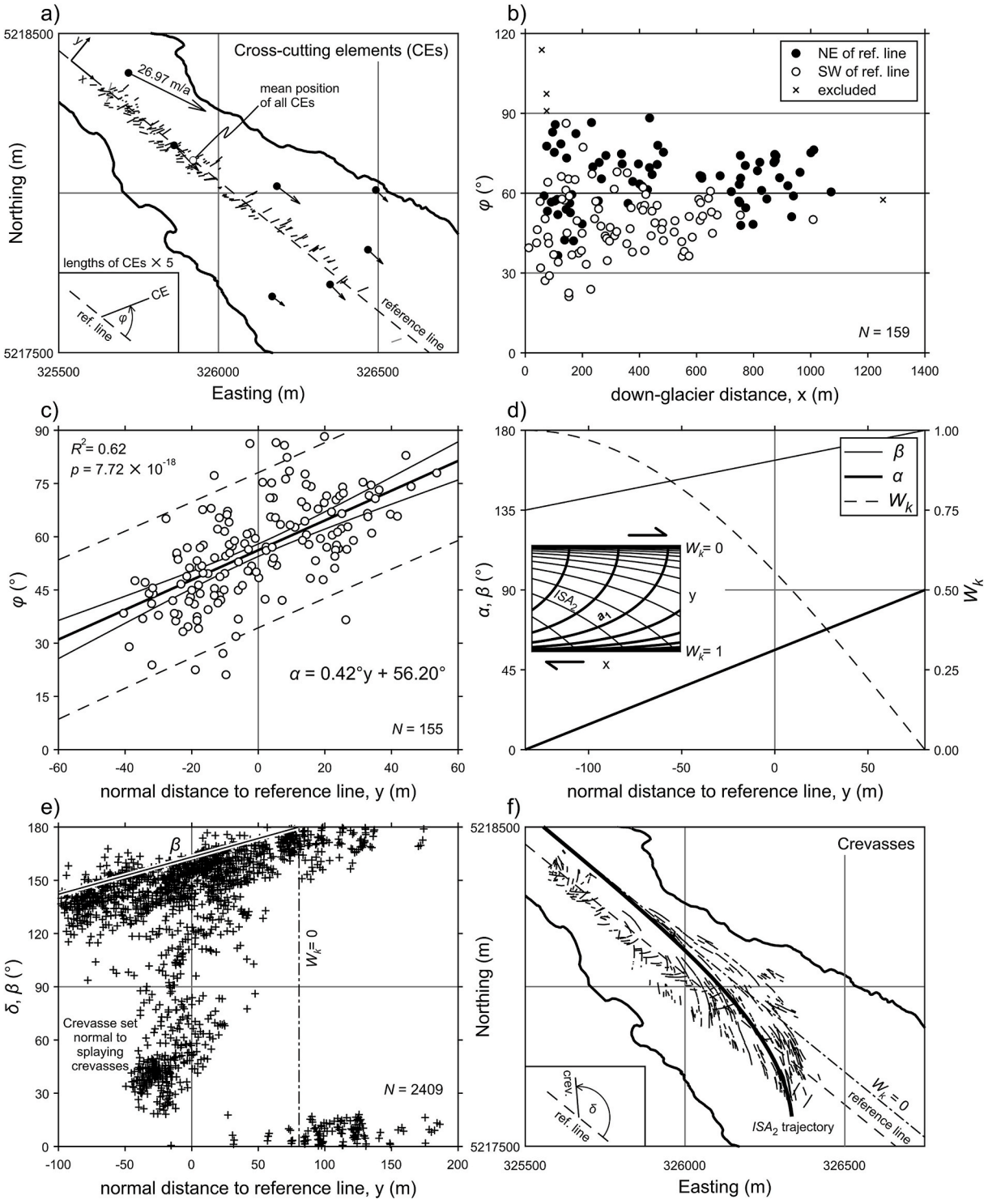

Fig. 8. Orientation analysis of cross-cutting elements (CEs) and crevasses. (a) Glacier outline, annual velocities (in m/a) and CE traces (lengths exaggerated × 5). White dot is mean position of all CEs and the dashed line is the reference line, whose orientation was obtained by optimising the correlation between the CEs' inclinations (φ; see inset) and the CEs' normal distances to that line (y), as shown in (c). (b) CE inclination vs. down-glacier distance. (c) Cross-plot of CE inclination vs. transverse distance, i.e. normal to reference line, together with the best-fit linear regression model and the 95% confidence belt around the data (dashed lines) and the regression (solid curves). (d) Plot of the flow characteristic orientations, α and β, and the kinematic vorticity, W_k, as a function of normal distance to the reference line, assuming that the best-fit relation given in (c) is an estimate for the inclination of the fabric attractor, i.e. $\varphi(y) \approx \alpha(y)$. Trajectories are constructed by simple integration (inset). (e) Cross-plot of crevasse inclination (δ; see inset in (f)) vs. normal distance to the reference line. The data are derived from the traces shown in Fig. 3a, where non-linear traces are discretised by linear segments, from which the centre and orientation are readily obtained. The theoretical inclination of the rate of maximum shortening (β), which should provide an upper bound to the crevasse inclinations, is also shown (same relation as in (d)). The theoretical position of the glacier's centreline, where splaying crevasses become longitudinal crevasses ($\delta = 180°$), is also shown ($W_k = 0$). (f) Glacier outline and interpreted crevasses, together with a theoretical ISA_2-trajectory, constructed by integration of the relation shown in (d). The theoretical glacier centreline is also shown ($W_k = 0$). See Section 6 for details.

(parabolic) flow profile, with a maximum velocity in the channel centre, mimicking the typical superficial velocity field of valley glaciers. The velocity gradients for such a radial velocity field are readily obtained, permitting visualising, for example, the trajectories of the flow eigenvectors ($\boldsymbol{a_1}$ and $\boldsymbol{a_2}$) and of the greatest instantaneous shortening axis (ISA_2), where the latter indeed resemble the traces of splaying crevasses (Fig. 9b). It is interesting to note that in this model the angle between ISA_2 and the margin is 45° in the absence of slip, whereas the angle decreases with increasing flow velocity at the boundary (relative to the central velocity). Finite strain ellipses show that the shear strain systematically increases from the centre to the margins and that pure shear is only present in the channel centre (Fig. 9c). Obviously, during progressive deformation the long axes of the strain ellipses become parallel to the fabric attractor ($\boldsymbol{a_2}$ for transtension). Both the flow characteristic orientations (Fig. 9b) and the finite strain distribution (Fig. 9c) are of course due to systematic variations of the kinematic vorticity, which increases from the channel centre ($W_k = 0$) towards the margins (Fig. 9d), where simple shear ($W_k = 1$) is only attained in the absence of slip. Even though this model is two-dimensional and lacks any mechanics, it is qualitatively consistent with the observed structures and the transverse variations of kinematic vorticity (Fig. 8).

7.2. Origin of flanking structures

As described in Section 3.4, the vast majority of flanking structures form around closed fractures or veins. In contrast to typical crevasse, or fracture, traces, which comprise layers of coarse clear ice ('blue bands'; see section 5.2.2. in Jennings and Hambrey, 2021, and references therein), the ice within the CEs is less translucent and has a smaller grainsize than in the surrounding ice and frequently exhibits a new foliation. These newly formed fabrics are consistent with slip on the CEs. Rarely, flanking structures form around small-scale moulins (Fig. 5a).

The mapped flanking structures are exposed within a relatively narrow zone along the right margin of the left flow unit (Fig. 2). Both their density and orientation variability decrease down-glacier (Fig. 8b). The absence of (mappable) flanking structures further NE most likely reflects that the rotation axis of initially sub-vertical crevasses is sub-horizontal in the left flow unit's central area, leading to flanking structures, if they do form, with sub-horizontal fold axes. Such flanking structures were indeed exposed on the fracture walls of longitudinal crevasses close to the Pasterze's terminus in the summer of 2016 (Fig. 10). Clearly, if similar flanking structures would be present further up-glacier, they would, in map view, fade into the foliation. The rare occurrence of flanking structures along the left margin on the other hand is probably due to low fracture density.

The high density and orientation variability of the CEs in the upper reaches of the zone reflects that CEs, or future CEs, are actively forming there and also up-glacier. Further down-glacier, the CEs orientation variability decreases and, as argued in Section 6, the majority of CEs have rotated into a stable orientation. However, it is doubtful that all CEs have originated in the upper reaches of the mapped area, since even stably orientated CEs continue to accommodate slip, which eventually leads to dismembering of the structure.

It is straightforward to estimate the rotation rate of a CE by assuming that it behaves like a passive marker line under a plane-strain homogenous transtensional background flow, as defined by Eq. (1). A constant rate of shear zone parallel shortening $\dot{e}$ leads, after a time t, to a shear zone parallel stretch $S = \exp(\dot{e}t)$. The components of a unit position vector at time $t = 0$ are $X = \cos\varphi_0$ and $Y = \sin\varphi_0$. Substitution of these initial positions into Eq. (3) gives the finite position for any given value of stretch, or time, so that the orientation of the line is given by:

$$\tan\varphi = \frac{\sin\varphi_0}{\cos\varphi_0 S^2 - \sin\varphi_0 \cot\alpha\left(S^2 - 1\right)}. \quad (6)$$

If one assumes that the CEs are fractures that form parallel to the greatest instantaneous shortening axis (ISA_2), i.e. $\varphi_0 = (\alpha + 270°)/2$, their orientation as a function of time can be determined. Curves of φ vs. time are shown in Fig. 11 for a range of values of α and for a shortening rate $\dot{e} = -15 \times 10^{-10}$ s^{-1}, a value taken from the upper reaches of the study area (see Fig. 2). These curves illustrate that CEs originating from fractures that formed parallel to the greatest shortening orientation have reached orientations of $\varphi < 90°$ after 7 ($\alpha = 30°$) to 21 years ($\alpha = 60°$). Typical flow velocities in the upper reaches of the study area are ca. 10 m/a, so that orientations of $\varphi < 90°$ are expected to develop after a down-glacier translation of 70–210 m. Theoretically, truly stable orientations are of course only achieved asymptotically as time goes to infinity. Hence curves on the plot (Fig. 11) indicate when the orientations are $\varphi \leq \alpha + 10°$ and $\varphi \leq \alpha + 5°$, where the time range for the former 'close-to-stable' orientation is 20 ($\alpha = 30°$) to 32 years ($\alpha = 60°$). Even though this simple analysis assumes a constant rate of shortening parallel to the flow direction and a constant vorticity, it illustrates that CEs forming up-glacier of or within the upper reaches of the study area will reach close-to-stable orientations after a few hundred metres of down-glacier translation. This crude estimate is consistent with the CE orientation vs. down-glacier distance plot (Fig. 8b), which shows that (i) unstable orientations ($\varphi > 90°$) only occur within the first 100 m and (ii) the range of orientations systematically decreases within the first 300–400 m of the flanking structure zone.

7.3. Transtensional vs. transpressional flanking structures in rocks

Plane strain transtension, as used throughout this paper, implies shortening parallel to the shear zone boundary (the 'tension' refers to the extension normal to the shear zone boundary). In the Earth's upper crust, transtension is expected to occur, for example, in fold and thrust belts, with shortening parallel to and extension (thickening) normal to a basal detachment. To date, the only and most convincing example of a transtensional s-type flanking fold from a fold-and-thrust belt (Tethyan Himalaya in Spiti, India) was described by Wiesmayr and Grasemann (2005) and is shown here again and compared with results of numerical modelling in Fig. 12a and b, respectively. The diagnostic features for transtension are as follows: (i) Reverse drag of the central marker line that passes into normal drag towards the CE's tips. (ii) Relatively large displacement of the central marker layer together with a pronounced displacement gradient towards the tips. (iii) Relatively large angle (37° in the example shown in Fig. 12a) of the CE with the passive markers, i.e. layering not affected by folding. Note that some s-type flanking folds in the Pasterze (Fig. 5g and h) exhibit the same features.

The geometrical differences between transpressional and transtensional s-type flanking folds are elucidated by an example from an oblique-slip normal shear zone in the Eastern Alps, which is kinematically constrained by co-existing a-type flanking folds and shear bands (Sölva et al., 2005), where the latter cannot form in transtension (Section 4). This transpressional s-type flanking fold (Fig. 12c and d) exhibits the following characteristics: (i) Normal drag of the central maker line that passes into reverse drag towards the CE's tips. (ii) A pronounced hook-shaped central marker line. (iii) Relatively small angle (16° in the example shown in Fig. 12c) of the CE with the shear zone boundary. The geometry of this transpressional flanking structure can be explained by the following progressive development, as suggested by numerical models of Grasemann et al. (2019): Initially antithetic shear along the CE formed an a-type flanking fold, but as the CE rotated, the central

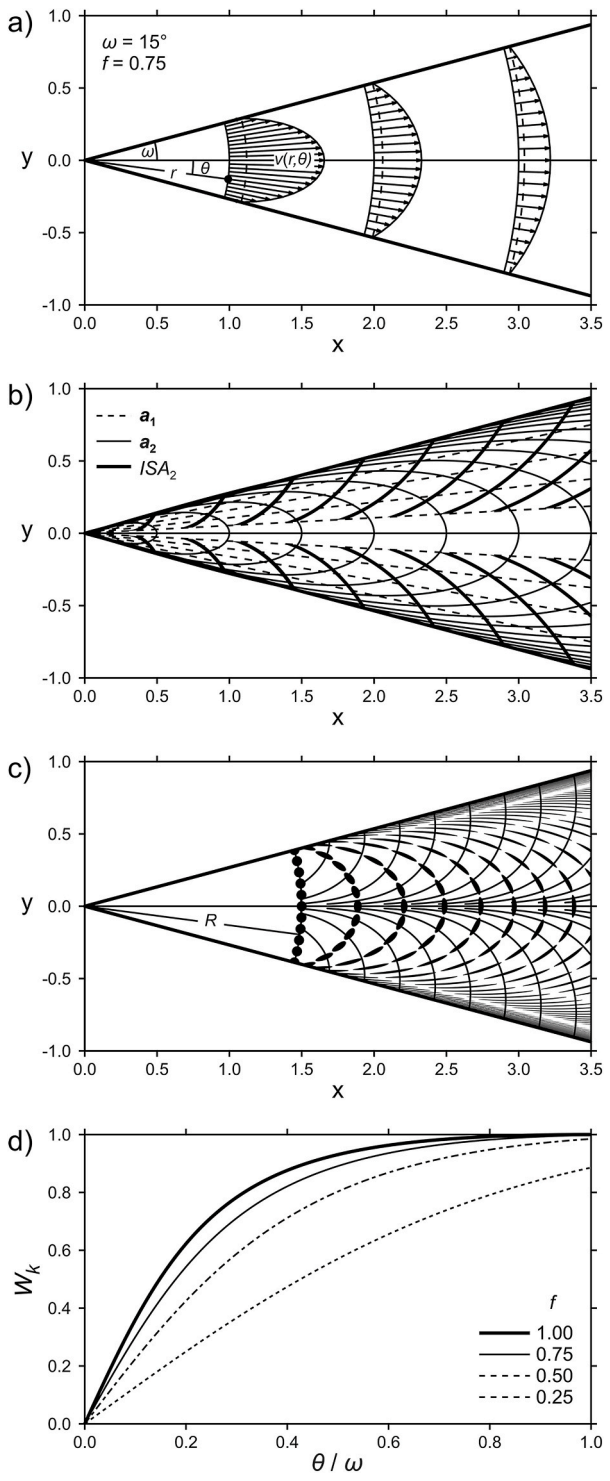

Fig. 9. Kinematic model of a diverging glacier of unit thickness (plane strain model). (a) Velocity field in polar coordinates. Vectors are shown at one-quarter of their actual size (for a flow rate of unity) at distances $r = 1$, 2 and 3. The dashed arcs show the uniform flow contribution. (b) Trajectories of orientations of eigenvectors of flow ($\boldsymbol{a}_1$ and $\boldsymbol{a}_2$) and greatest rate of shortening (ISA_2). For clarity, the latter are not shown in central area. (c) Strain ellipses for circles initially located at a distance $R = 1.5$ in dimensionless time intervals $\Delta t = 0.25$. Also shown are trajectories of the short axes of the finite strain ellipses. (d) Kinematic vorticity vs. normalised polar angle for four values of f. For $f = 1$ the velocity profile is purely quadratic. For $f = 0$ the velocity profile is uniform and $W_k = 0$ (pure shear) everywhere. See Appendix D for details.

marker's offset eventually switched from anti-to synthetic. This development results in reverse drag and markers with a prominent hook-shape (Hudleston, 1989) or over-roll (Coelho et al., 2005) of the central marker line.

7.4. Transtensional vs. transpressional ductile shear zones

Transpression/transtension kinematics is a direct consequence of the rotational character of plate tectonics (Harland, 1971; Dewey et al., 1998) and the theoretical fabric development under transpression/transtension, including more complex non-plane strain types, has received much attention over the last decades (Sanderson and Marchini, 1984; Tikoff and Fossen, 1993; Robin and Cruden, 1994; Fossen and Tikoff, 1998). However, the ubiquity of shear bands and a-type flanking folds and the general lack of s-type flanking folds with geometries typical for transtension (e.g., Fig. 12a and b) in natural ductile shear zones raises some questions about the occurrence of transtensional shear. In fact, there are numerous examples of ductile shear zones from various tectonic settings for which quantitative strain analysis indicates transpressional flow (Talbot and Sokoutis, 1995; Tikoff and Green, 1997; Grasemann et al., 1999; Lin and Jiang, 2001; Czeck and Hudleston, 2003; Xypolias et al., 2003, 2018; Sengupta and Ghosh, 2004; Goscombe et al., 2005; Passchier et al., 2007; Sullivan and Law, 2007; Sarkarinejad et al., 2008; Gillam et al., 2013; Little et al., 2016; Carreras and Druguet, 2019). In contrast, transtensional flow in ductile shear zones is rarely deduced and typically supported by conceptual models derived from independent geological arguments (Krabbendam and Dewey, 1998; Whitney et al., 2007; Erkül et al., 2017). Furthermore, quantitative vorticity analyses suggest that the majority of investigated ductile shear zones record a transpressional flow (for a review see Xypolias, 2010, and references cited therein). However, transtensional deformation must occur, for example, at the large scale within releasing bends of crustal strike-slip zones (Harding, 1985; Dewey et al., 1998; Waldron, 2005) and can also be inferred at a small-scale from the initiation angle of en échelon veins in brittle-ductile shear zones (Ramsay and Huber, 1983; Peacock and Sanderson, 1995). Nevertheless, even in extensional tectonic settings, there is strong evidence that shear zones along detachment systems follow a transpressional deformation path (Bailey and Eyster, 2003) and are characterized by pervasive shear band fabrics at various scales (e.g., Jolivet et al., 2010) or mechanically interact with rotating high-angle faults (Wernicke 1981; Lister et al., 1984; Gessner et al., 2001), indicating that these crustal scale extensional shear zones are stretching faults (Means, 1989).

The sparseness of reported transtensional ductile shear zones hence raises the question: Is transtensional flow in the Earth's crust rare or were the kinematics of certain shear zones misinterpreted? Perhaps the natural and modelled transtensional flanking structures presented in this study (ideally in conjunction with clast system analysis; Simpson and De Paor, 1993; Marques and Coelho, 2003) serve as an aid to better interpret the kinematics of natural shear zones, so that in the future this question can be answered.

8. Conclusions

Analysis and modelling of transtensional flanking structures exposed in an alpine valley glacier led to the following conclusions:

- The most frequently observed flanking structures in the glacier are a-type flanking folds with an antithetic offset. The cross-cutting elements (CEs), which are typically closed crevasses, are generally inclined into the overall map-view shear flow.
- Shear bands, which are entirely absent in the studied area, appear to be unstable under transtensional general shear. Although the absence of shear bands is not necessarily an indicator for transtension, since they can only form along CEs inclined against the

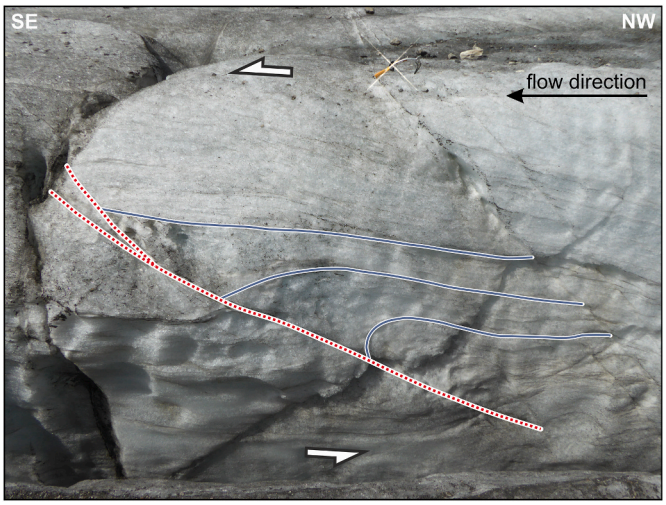

Fig. 10. Flanking structure exposed in a vertical longitudinal crevasse SE of the mapped area, near the glacier centre line and close to the glacier terminus (26/07/2016; UTM33 327730E 5216760N; ice pick for scale). At the time of writing the glacier terminus is located NW of this area. The foliation dips moderately up-glacier, i.e. towards the NW. In the hanging wall of the CE, a pronounced normal drag passes updip into a reverse drag. Correlation of the foliation across the CE is ambiguous, the footwall is hence uninterpreted. The fold axis is sub-horizontal, which was confirmed by inspecting the same structure on the opposite crevasse wall. The flanking folds most likely formed by counter-clockwise rotation of the CE around a sub-horizontal axis, or more precisely, co-rotation of the CE under top-SE shearing due to upwards increase of ice-flow velocity. Uninterpreted photo is provided as an electronic supplement.

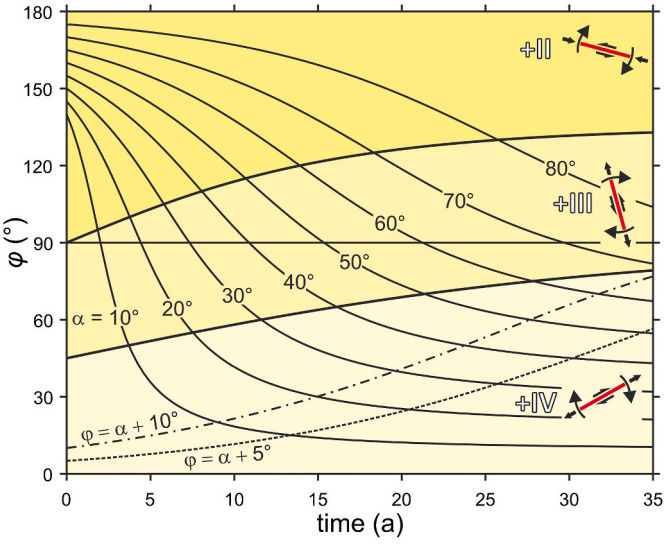

Fig. 11. Graph illustrating the orientation of passive marker lines as a function of time (Eq. (6)) for a range of α-values under plane-strain transtension with a constant shear zone parallel shortening rate of $\dot{e} = -15 \times 10^{-10}\ s^{-1}$. The initial orientation at $t = 0$ is, for each value of α, parallel to the orientation of ISA_2, i.e. $\varphi_0 = (\alpha + 270°)/2$. Fields of instantaneous behaviour are coloured and labelled as in Fig. 6, with the CE kinematics shown for dextral transtensional background shear. The dash-dot and dashed curves labelled $\varphi \leq \alpha + 10°$ and $\varphi \leq \alpha + 5°$ indicate when a passive marker has reached a 'close-to-stable' orientation.

overall shear, an abundance of shear bands is a diagnostic feature for transpressional general shear.

- The angle between the CEs and the glacier's flow direction systematically increases in a transverse direction towards the glacier's centreline. Under the assumption that the CEs have reached, on average, a stable orientation, the kinematic vorticity and the orientation of the maximum shortening rate can be determined. Trajectories of the latter are sub-parallel to the glacier's splaying crevasses, indicating that they nucleate parallel to the greatest compressive stress orientation.
- The observed flanking structure geometries, the spatial variation of CE orientations, the absence of shear bands and the geometry of the splaying crevasses are consistent with plane-strain transtensional shear, caused primarily by down-glacier valley widening.
- The abundance of shear bands in natural ductile shear zones in rock indicates that transpression may be more common than transtension, but perhaps transtensional shear zones have been misinterpreted. The natural and modelled transtensional flanking structures presented in this study (ideally in conjunction with clast system analysis) hopefully serve as an aid to better interpret the kinematics of natural shear zones.

Author Statement

Franziska Mayrhofer: Data curation; Formal analysis; Investigation; Methodology; Visualization; Writing - original draft; **Martin Schöpfer**: Conceptualization; Formal analysis; Investigation; Methodology; Supervision; Visualization; Writing - review & editing; **Marta Adamuszek**: Investigation; Methodology; Software; Visualization; **Marcin Dąbrowski**: Investigation; Methodology; Software; **Bernhard Grasemann**: Conceptualization; Formal analysis; Investigation; Methodology; Project administration; Resources; Supervision; Visualization; Writing - review & editing;

Declaration of competing interest

The authors declare that they have no known competing financial interests or personal relationships that could have appeared to influence the work reported in this paper.

Acknowledgments

We acknowledge the Zentralanstalt für Meteorologie und Geodynamik (ZAMG) for sharing their annual stake measurements and permission to publish them, the Großglockner-Hochalpenstraßen for granting discounted annual tickets, and both the Österreichischer Alpenverein and the Nationalpark Hohe Tauern for permission to conduct the study. We thank Ulrike Pistotnik for arranging permission to do the research. Daniel Le Heron, Anna Rogowitz, Lars Scharfenberg and Arian Wawra are acknowledged for field assistance and discussions. We are grateful to Paul Herbst for introducing us to the structures in the Pasterze and for many discussions over the past years. We express thanks to Wolfgang Schöner for providing guidance throughout the course of this project. We thank Toni and Cäcilia from the Karl Volkert Haus for their hospitality and the most-needed post-fieldwork gourmet dinners. Thorough and useful reviews delivered by Peter Hudleston and an anonymous reviewer and the editorial handling by Ian Alsop are acknowledged.

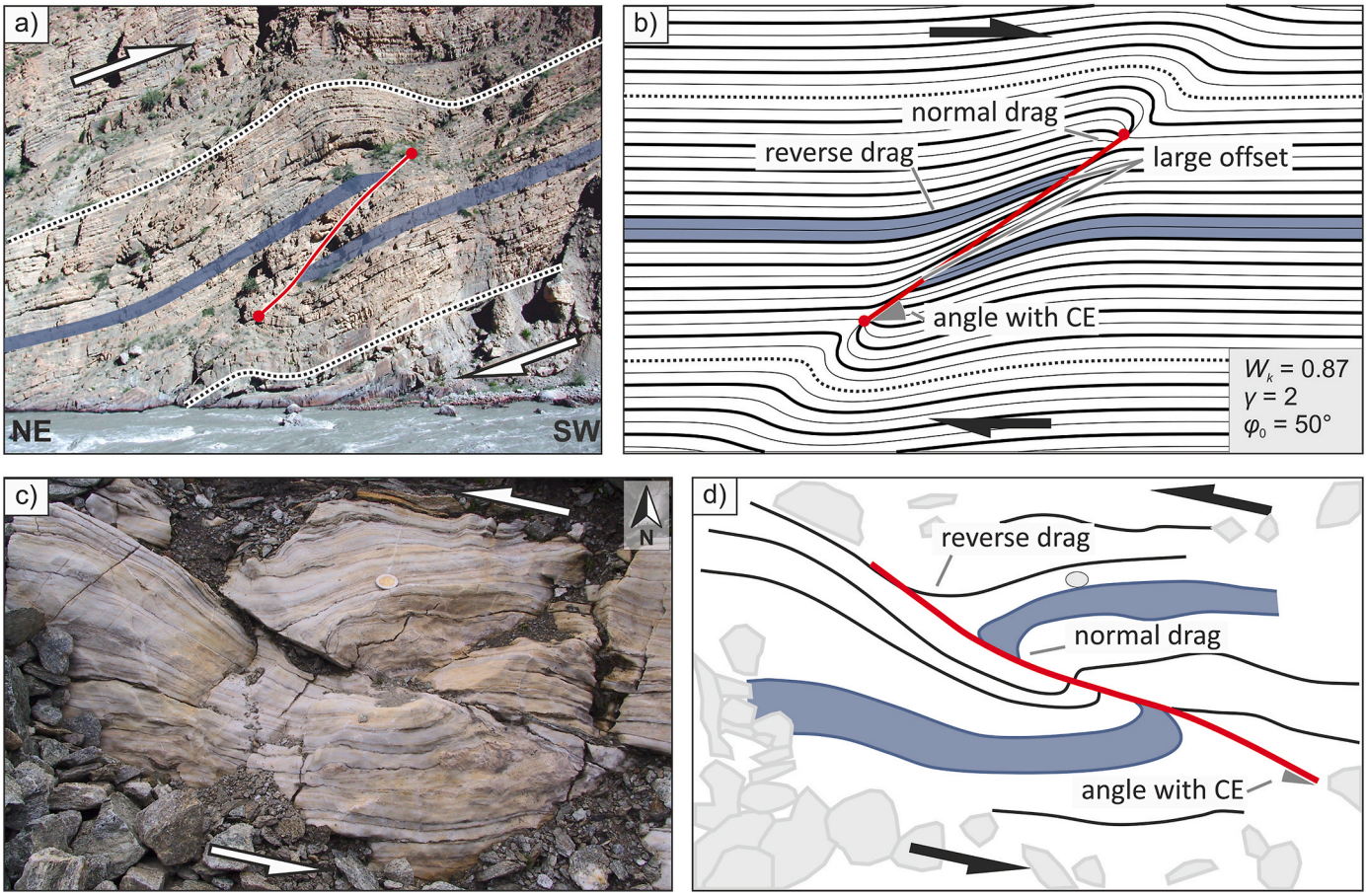

Fig. 12. Examples and diagnostic features of transtensional and transpressional s-type flanking folds. (a) Flanking structure within Jurassic limestones exposed in the Pin Valley in Spiti, N-India (UTM44 231570E, 3554201N), interpreted to have formed due to top SW transtensional shearing (from Wiesmayr and Grasemann, 2005) (b) Numerical model of a flanking structure formed under progressive transtensional shear with a kinematic vorticity $W_k = 0.87$, after an apparent shear strain $\gamma = 2$ (see Fig. 7). The CE's initial inclination relative to the shear zone boundary was $\varphi_0 = 50°$ and it rotated to an inclination close to the fabric attractor ($\alpha = 30°$). (c) Natural example of a s-type flanking fold within marbles of the Schneeberger Zug in the Eastern Alps (UTM32 654808E, 5180005N), interpreted to have formed due to sinistral transpressional shearing. (d) Line drawing of the structure shown in (c), highlighting certain characteristic features. See Section 7.3 for discussion.

Supplementary data

Supplementary data to this article can be found online at https://doi.org/10.1016/j.jsg.2022.104659.

Appendix A. Structure from Motion and drone flight parameters

The aerial photo shown in Fig. 2 is an orthopicture (WGS84/UTM zone 33N) draped with global opacity of 70% on the hillshade of a digital elevation model (DEM) using the software QGis 3.20.3 (qgis.org). Both the DEM and the orthopicture were generated from 790 aerial photos taken on July 13 2020 with a Hasselblad L1D-20c of a DJI Mavic 2 Pro UAV (F-stop F/8, ISO 100, Shutter 1/1000; for technical details see www.dji.com). The drone was flying at an altitude of 30 m above the glacier in an automatic grid mission, which was planned using the PIX4Dcapture mapping app (www.pix4d.com). The camera had a tilt angle of 70° and the flight plan guaranteed an overlap of the pictures of 80%. A dense point cloud with 363,184,437 points was calculated from the aerial pictures using the photogrammetric software Agisoft Metashape Professional 1.7.3 (www.agisoft.com). The dense point cloud was used as the source to calculate with Agisoft a DEM with a resolution of 5.19 cm/pix and an orthomosaic with a resolution of 2.6 cm/pix.

Appendix B. Annual velocities and strain rate calculations

The Pasterze glacier is subjected to mass balance monitoring programs conducted by the Zentralanstalt für Meteorologie und Geodynamik (ZAMG), which is measuring and maintaining a network of stakes drilled into the ice. For the present study, a selection of stakes, whose positions are determined annually using dGPS, was used for computing annual strain rates for the time interval July 2018 to July 2019 (Table B1). The initial stake positions were triangulated and for each triangle the average strain rate tensor was computed as follows.

The position vector $\boldsymbol{x}$ after deformation and translation as a function of the initial position vector $\boldsymbol{X}$ is given by

$$\boldsymbol{x} = \boldsymbol{F}\boldsymbol{X} + \boldsymbol{T} \tag{B1}$$

Table B1
Easting (X, x) and northing (Y, y) of stake positions (in meters; UTM 33) in July 2018 (X, Y) and July 2019 (x, y). 'ZAMG' is the designation used by the Zentralanstalt für Meteorologie und Geodynamik, whereas 'No.' is the number used in the present study. The following stake combinations where used for the strain rates given in Fig. 2: 1–2–3; 1–3–7; 2–3–4; 3–4–5; 3–5–6; 3–6–7; 4–5–8; 5–6–9; 6–7–9.

ZAMG	No.	X	Y	x	y
37–18	1	402208.047	217632.290	402232.196	217620.271
29–18	2	402372.351	217404.063	402380.002	217396.093
GPS-18	3	402697.130	217280.654	402704.276	217275.178
11–17	4	402692.921	216932.103	402696.718	216929.221
27–18	5	402872.614	216975.144	402877.253	216970.430
21–18	6	402988.845	217086.592	402993.495	217082.165
22–18	7	403010.565	217273.341	403014.212	217269.735
35–18	8	403083.010	216481.652	403087.573	216479.755
18–18	9	403435.788	216752.848	403440.185	216750.643
17–18	10	403646.143	216519.305	403649.630	216517.604
AWS-18	11	403706.246	216300.073	403710.127	216299.883
16–18	12	403838.599	216115.651	403841.589	216115.452
33–18	13	404313.506	215566.278	404317.044	215567.850
04–18	14	404294.736	215967.125	404296.193	215967.897

where $\boldsymbol{F}$ is the deformation gradient tensor and $\boldsymbol{T}$ is the translation. For three position vectors (subscripts 1–3) this relation can be written as

$$\begin{pmatrix} x_1 \\ x_2 \\ x_3 \end{pmatrix} = \boldsymbol{M} \begin{pmatrix} F_{xx} \\ F_{xy} \\ T_x \end{pmatrix}, \quad \begin{pmatrix} y_1 \\ y_2 \\ y_3 \end{pmatrix} = \boldsymbol{M} \begin{pmatrix} F_{yx} \\ F_{yy} \\ T_y \end{pmatrix}, \quad \boldsymbol{M} = \begin{pmatrix} X_1 & Y_1 & 1 \\ X_2 & Y_2 & 1 \\ X_3 & Y_3 & 1 \end{pmatrix} \tag{B2}$$

These are two systems of linear equations, which can be solved easily. The velocity gradient tensor $\boldsymbol{L}$ and the translation rate $\dot{\boldsymbol{T}}$ are given by

$$\boldsymbol{L} = \ln(\boldsymbol{F})/\Delta t, \ \dot{\boldsymbol{T}} = \boldsymbol{T}/\Delta t \tag{B3}$$

where ln is the matrix logarithm and Δt the time interval between $\boldsymbol{X}$ and $\boldsymbol{x}$. The strain rate tensor is given by

$$\boldsymbol{E} = \frac{1}{2}\left(\boldsymbol{L} + \boldsymbol{L}^{\mathrm{T}}\right) \tag{B4}$$

The eigenvalues of $\boldsymbol{E}$ are the principal strain rates and the eigenvectors of $\boldsymbol{E}$ are the principal strain rate axes (as plotted in Fig. 2).

Appendix C. Semi-analytical solution of the progressive evolution of flanking structures

A semi-analytical approach, similar to the method described in Kocher and Mancktelow (2005), is used to model flanking structures under monoclinic shear. For any given flow conditions in the far field and the instantaneous orientation of the cross-cutting element, the velocity field in the matrix is computed using an analytical solution implemented in MATLAB (www.mathworks.com). The cross-cutting element is modelled as an essentially frictionless, highly elongated and flattened ellipsoidal inclusions that mimics a blade crack. The inclusion is embedded in an isotropic linear viscous matrix and the velocity computation is based on a reduced version of the external Eshelby solution (Eshelby, 1959), which is explicitly adjusted for material incompressibility. More details on the solution technique are given in Exner and Dabrowski (2010) and Adamuszek and Dabrowski (2017). Flanking structures evolution is tracked with a set of initially horizontal material lines that are passively deformed due to flow perturbation around the cross-cutting element. Material advection is computed using the highly accurate, adaptive numerical solver 'ode45', as implemented in MATLAB.

Appendix D. Plane strain kinematic model of a widening channel

A widening 'glacier' is kinematically modelled in 2D (assuming constant unit thickness, i.e. $\partial v_z/\partial z = 0$) by defining a radial velocity field $v_r(r, \theta)$ in polar coordinates, where $r = \sqrt{x^2 + y^2}$ and $\theta = \tan^{-1}(y/x)$, within a circular sector of central half-angle ω.

A 'quadratic' velocity profile of unit flow rate is given by

$$v_r^{(q)} = \frac{3}{4\omega r}\left(1 - \phi^2\right) \tag{D1}$$

where $\phi = \theta/\omega$ is the normalised polar angle. A uniform velocity profile of unit flow rate is given by

$$v_r^{(u)} = \frac{1}{2\omega r} \tag{D2}$$

These two profiles may be combined by introducing a weighting factor $f[0,1]$, so that the total velocity profile is given by

$$v_r = f v_r^{(q)} + (1-f) v_r^{(u)} = \frac{f\left(1-3\phi^2\right)+2}{4\omega r} \tag{D3}$$

so that for $f = 1$ the velocity profile is quadratic, for $f = 0$ the velocity profile is uniform and for $0 < f < 1$ the velocity profile is a combination of the two.

The velocity gradient tensor in polar coordinates, $\boldsymbol{L_p}$, is given by

$$\boldsymbol{L_p} = \begin{bmatrix} \frac{\partial v_r}{\partial r} & \frac{1}{r}\frac{\partial v_r}{\partial \theta} - \frac{v_\theta}{r} \\ \frac{\partial v_\theta}{\partial r} & \frac{1}{r}\frac{\partial v_\theta}{\partial \theta} + \frac{v_r}{r} \end{bmatrix} \tag{D4}$$

In the present case the velocity field is purely radial, i.e. $v_r(r,\theta)$ and $v_\theta = 0$, so that the velocity gradient tensor simplifies to

$$\boldsymbol{L_p} = \begin{bmatrix} \frac{\partial v_r}{\partial r} & \frac{1}{r}\frac{\partial v_r}{\partial \theta} \\ 0 & \frac{v_r}{r} \end{bmatrix} \tag{D5}$$

Differentiating the radial velocity with respect to r and θ yields (recall that $\phi(\theta)$)

$$\frac{\partial v_r}{\partial r} = -\frac{f\left(1-3\phi^2\right)+2}{4\omega r^2} \tag{D6a}$$

$$\frac{\partial v_r}{\partial \theta} = -\frac{3f\phi}{2\omega^2 r} \tag{D6b}$$

The continuity equation for an incompressible fluid reads

$$\frac{\partial v_r}{\partial r} + \frac{1}{r}\frac{\partial v_\theta}{\partial \theta} + \frac{v_r}{r} = 0 \tag{D7}$$

which, upon substitution of the above relations, confirms that the deformation is isochoric.

The velocity gradient tensor is hence defined in polar coordinates and can be readily converted to Cartesian coordinates via

$$\boldsymbol{L} = \boldsymbol{R}\boldsymbol{L_p}\boldsymbol{R}^T \tag{D8}$$

where

$$\boldsymbol{R} = \begin{bmatrix} \cos\theta & -\sin\theta \\ \sin\theta & \cos\theta \end{bmatrix} \tag{D9}$$

The (unit) eigenvectors of $\boldsymbol{L}$ are $\boldsymbol{a}_1$ and $\boldsymbol{a}_2$ and the kinematic vorticity is $W_k = \boldsymbol{a}_1 \cdot \boldsymbol{a}_2 = \cos\alpha$. The strain rate and the spin tensor are given by

$$\boldsymbol{E} = \frac{1}{2}\left(\boldsymbol{L} + \boldsymbol{L}^{\mathrm{T}}\right) \tag{D10a}$$

$$\boldsymbol{W} = \frac{1}{2}\left(\boldsymbol{L} - \boldsymbol{L}^{\mathrm{T}}\right) \tag{D10b}$$

where the eigenvalues and vectors of $\boldsymbol{E}$ are the principal strain rates and their orientations ($ISA_{1,2}$) in Cartesian coordinates.

Finite positions after a time t within the wedge-shaped region can be readily determined (e.g., for circles, passive markers, etc.) by noting that velocity is the time derivative of displacement with respect to time,

$$v_r = \frac{\partial r}{\partial t} = \frac{f\left(1-3\phi^2\right)+2}{4\omega r} \tag{D11}$$

which is an ordinary differential equation with the solution

$$r = \sqrt{2}\left[\frac{R^2}{2} + t\frac{f\left(1-3\phi^2\right)+2}{4\omega}\right]^{1/2} \tag{D12}$$

where R is the initial and r the finite position (for a given polar angle θ). The deformation gradient tensor in polar coordinates with respect to the reference coordinate system (R,θ) is, for a purely radial displacement field, given by

$$\boldsymbol{F_p} = \begin{bmatrix} \frac{\partial r}{\partial R} & \frac{1}{R}\frac{\partial r}{\partial \theta} \\ 0 & \frac{r}{R} \end{bmatrix} \tag{D13}$$

which can be easily converted to Cartesian coordinates via $\boldsymbol{F} = \boldsymbol{R}\boldsymbol{F_p}\boldsymbol{R}^{\mathrm{T}}$, although the components of $\boldsymbol{F}$ are rather lengthy and not given here. The left Cauchy-Green strain, also known as Finger tensor, is

$$\boldsymbol{b} = \boldsymbol{F}\boldsymbol{F}^{\mathrm{T}} \tag{D14}$$

The eigenvalues of $\boldsymbol{b}$ are the principal quadratic elongations and the eigenvectors of $\boldsymbol{b}$ give the orientations of the axes of the finite strain ellipse in Cartesian coordinates.

References

Adamuszek, M., Dabrowski, M., 2017. Sheath fold development in monoclinic shear zones. Terra Nova 29, 356–362.

Bai, T., Maerten, L., Gross, M., Aydin, A., 2002. Orthogonal cross joints: do they imply a regional stress rotation? J. Struct. Geol. 24, 77–88.

Bailey, C.M., Eyster, E.L., 2003. General shear deformation in the Pinaleño Mountains metamorphic core complex, Arizona. J. Struct. Geol. 25, 1883–1892.

Bobyarchick, A.R., 1986. The eigenvalues of steady flow in Mohr space. Tectonophysics 122 (1–2), 35–51.

Carreras, J., Druguet, E., 2019. Complex fold patterns developed by progressive deformation. J. Struct. Geol. 125, 195–201.

Coelho, S., Passchier, C., Grasemann, B., 2005. Geometric description of flanking structures. J. Struct. Geol. 27, 597–606.

Czeck, D.M., Hudleston, P.J., 2003. Testing models for obliquely plunging lineations in transpression: a natural example and theoretical discussion. J. Struct. Geol. 25, 959–982.

De Paor, D.G., Means, W.D., 1984. Mohr circles of the First and Second Kind and their use to represent tensor operations. J. Struct. Geol. 6, 693–701.

Dewey, J.F., Holdsworth, R.E., Strachan, A., 1998. Transpression and transtension zones. In: Holdsworth, R.E., Strachan, R.A., Dewey, J.F. (Eds.), Continental Transpressional and Transtensional Tectonics. Geol. Soc. Lond. Spec. Pub., 135 Geological Society of London, pp. 1–14.

Erkül, F., Tatar Erkül, S., Manap, H.S., Çolak, C., 2017. An extensional and transtensional origin of elongated magmatic domes and localised transfer faults in the northern Menderes metamorphic core complex, western Turkey. Geodin. Acta 29, 139–159.

Eshelby, J.D., 1959. The elastic field outside an ellipsoidal inclusion. Proc. Royal Soc. A 252, 561–569.

Exner, U., Dabrowski, M., 2010. Monoclinic and triclinic 3D flanking structures around elliptical cracks. J. Struct. Geol. 32, 2009–2021.

Exner, U., Grasemann, B., Mancktelow, N.S., 2006. Multiple faults in ductile simple shear: analogue models of flanking structure systems. In: Buiter, S.J.H., Schreurs, G. (Eds.), Analogue and Numerical Modelling of Crustal-Scale Processes. Geol. Soc. Lond. Spec. Pub., 253 Geological Society of London, pp. 381–395.

Exner, U., Mancktelow, N.S., Grasemann, B., 2004. Progressive development of s-type flanking folds in simple shear. J. Struct. Geol. 26, 2191–2201.

Fletcher, R.C., 2009. Deformable, rigid, and inviscid elliptical inclusions in a homogeneous incompressible anisotropic viscous fluid. J. Struct. Geol. 31, 382–387.

Fossen, H., Tikoff, B., 1998. Extended models of transpression and transtension, and application to tectonic settings. In: Holdsworth, R.E., Strachan, R.A., Dewey, J.F. (Eds.), Continental Transpressional and Transtensional Tectonics. Geol. Soc. Lond. Spec. Pub., 135 Geological Society of London, pp. 15–33.

Fossen, H., Tikoff, T.B., Teyssier, C., 1994. Strain modeling of transpressional and transtensional deformation. Nor. Geol. Tidsskr. 74, 134–145.

Gessner, K., Ring, U., Johnson, C., Hetzel, R., Passchier, C.W., Güngör, T., 2001. An active bivergent rolling-hinge detachment system: central Menderes metamorphic core complex in western Turkey. Geology 29, 611–614.

Gillam, B.G., Little, T.A., Smith, E., Toy, V.G., 2013. Extensional shear band development on the outer margin of the Alpine mylonite zone, Tatare Stream, Southern Alps, New Zealand. J. Struct. Geol. 54, 1–20.

Glen, J.W., 1955. The creep of polycrystalline ice. Proc. Roy. Soc. Lond. A 228, 519–538.

Goscombe, B.E.N., Gray, D., Hand, M., 2005. Extrusional tectonics in the core of a transpressional orogen; the Kaoko belt, Namibia. J. Petrol. 46, 1203–1241.

Grasemann, B., Stüwe, K., 2001. The development of flanking folds during simple shear and their use as kinematic indicators. J. Struct. Geol. 23, 715–724.

Grasemann, B., Fritz, H., Vannay, J.-C., 1999. Quantitative kinematic flow analysis from the Main Central Thrust Zone (NW-Himalaya, India); implications for a decelerating strain path and the extrusion of orogenic wedges. J. Struct. Geol. 21, 837–853.

Grasemann, B., Stüwe, K., Vannay, J.-C., 2003. Sense and non-sense of shear in flanking structures. J. Struct. Geol. 25, 19–34.

Grasemann, B., Dabrowski, M., Schöpfer, M.P.J., 2019. Sense and non-sense of shear reloaded. J. Struct. Geol. 125, 20–28.

Gspurning, J., Tintor, W., Tribuser, M., Wakoningg, H., 2004. Volumen- und Flächenänderungen an der Pasterze von 1981 bis 2000. Carinthia II 194/114, pp. 463–472.

Hamblin, W.K., 1965. Origin of "reverse drag" on the down-thrown side of normal faults. Geol. Soc. Am. Bull. 76, 1145–1164.

Hambrey, M.J., 1975. The origin of foliation in glaciers: evidence from some Norwegian examples. J. Glaciol. 14 (70), 181–185.

Hambrey, M.J., 1977. Foliation, minor folds and strain in glacier ice. Tectonophysics 39 (1–3), 397–416.

Hambrey, M.J., Lawson, W., 2000. Structural styles and deformation fields in glaciers: a review. In: Maltman, A.J., Hubbard, B., Hambrey, M.J. (Eds.), Deformation of Glacial Materials. Geol. Soc. Lond. Spec. Pub., 176 Geological Society of London, pp. 59–83.

Hambrey, M.J., Milnes, A.G., 1975. Boudinage in glacier ice - some examples. J. Glaciol. 14 (72), 383–393.

Harding, T.P., 1985. Seismic characteristics and identification of negative flower structures, positive flower structures, and positive structural Inversion1. AAPG (Am. Assoc. Pet. Geol.) Bull. 69, 582–600.

Harland, W.B., 1971. Tectonic transpression in Caledonian Spitsbergen. Geol. Mag. 108, 27–42.

Harper, J., Humphrey, N., Pfeffer, W., 1998. Crevasse patterns and the strain-rate tensor: a high-resolution comparison. J. Glaciol. 44 (146), 68–76.

Herbst, P., Neubauer, F., 2000. The Pasterze glacier, Austria: an analogue of an extensional allochthon. In: Maltman, A.J., Hubbard, B., Hambrey, M.J. (Eds.), Deformation of Glacial Materials. Geol. Soc. Spec. Publ., 176 Geological Society of London, pp. 159–168.

Herbst, P., Neubauer, F., Schöpfer, M.P.J., 2006. The development of brittle structures in an alpine valley glacier: Pasterzenkees, Austria, 1887-1997. J. Glaciol. 52, 128–136.

Hooke, R.L., 2019. Principles of Glacier Mechanics, third ed. Cambridge University Press, Cambridge.

Hooke, R.L., Hudleston, P.J., 1978. Origin of foliation in glaciers. J. Glaciol. 20 (83), 285–299.

Hudleston, P.J., 1989. The association of folds and veins in shear zones. J. Struct. Geol. 11, 949–957.

Hudleston, P.J., 2015. Structures and fabrics in glacial ice: a review. J. Struct. Geol. 81, 1–27.

Jennings, S.J.A., Hambrey, M.J., 2021. Structures and deformation in glaciers and ice sheets. Rev. Geophys. 59 (3), e2021RG000743.

Jolivet, L., Lecomte, E., Huet, B., Denèle, Y., Lacombe, O., Labrousse, L., Le Pourhiet, L., Mehl, C., 2010. The North Cycladic Detachment System. Earth Planet Sci. Lett. 289, 87–104.

Kamb, B., Raymond, C.F., Harrison, W.D., Engelhardt, H., Echelmeyer, K.A., Humphrey, N., Brugman, M.M., Pfeffer, T., 1985. Glacier surge mechanism: 1982-1983 surge of Variegated Glacier, Alaska. Science, New Series 227, 469–479.

Kaufmann, V., Kellerer-Pirklbauer, A., Lieb, G.K., Slupetzky, H., Avian, M., 2015. Glaciological studies at Pasterze glacier (Austria) based on aerial photographs. In: Li, J., Yang, X. (Eds.), Monitoring and Modeling of Global Changes: A Geomatics Perspective. Springer Netherlands, Dordrecht, pp. 173–198.

Kellerer-Pirklbauer, A., Kulmer, B., 2019. The evolution of brittle and ductile structures at the surface of a partly debris-covered, rapidly thinning and slowly moving glacier in 1998–2012 (Pasterze Glacier, Austria). Earth Surf. Process. Landforms 44, 1034–1049.

Kellerer-Pirklbauer, A., Lieb, G.K., Avian, M., Gspurning, J., 2008. The response of partially debris-covered valley glaciers to climate change: the example of the Pasterze Glacier (Austria) in the period 1964 to 2006. Geogr. Ann.: Series A 90 (4), 269–285.

Kocher, T., Mancktelow, N., 2005. Dynamic reverse modelling of flanking structures: a source of quantitative kinematic information. J. Struct. Geol. 27, 1346–1354.

Kocher, T., Mancktelow, N., 2006. Flanking structure development in anisotropic viscous rock. J. Struct. Geol. 28, 1139–1145.

Krabbendam, M., Dewey, J.F., 1998. Exhumation of UHP rocks by transtension in the Western Gneiss Region, Scandinavian Caledonides. In: Holdsworth, R.E., Strachan, R.A., Dewey, J.F. (Eds.), Continental Transpressional and Transtensional Tectonics. Geol. Soc. Spec. Publ., 135 Geological Society of London, pp. 159–181.

Lawson, W.J., Sharp, M.J., Hambrey, M.J., 1994. The structural geology of a surge-type glacier. J. Struct. Geol. 16, 1447–1462.

Lieb, G.K., Slupetzky, H., 2011. Die Pasterze. Der Gletscher am Grossglockner. Verlag Anton Pustet, Salzburg, Austria.

Lin, S., Jiang, D., 2001. Using along-strike variation in strain and kinematics to define the movement direction of curved transpressional shear zones: an example from northwestern Superior Province, Manitoba. Geology 29 (9), 767–770.

Lin, S., Jiang, D., Williams, P.F., 1998. Transpression (or transtension) zones of triclinic symmetry: natural example and theoretical modelling. In: Holdsworth, R.E., Strachan, R.A., Dewey, J.F. (Eds.), Continental Transpressional and Transtensional Tectonics. Geol. Soc. Spec. Publ., 135 Geological Society of London, pp. 41–57.

Lister, G.S., Banga, G., Feenstra, A., 1984. Metamorphic core complexes of Cordilleran type in the Cyclades, Aegean Sea, Greece. Geology 12, 221–225.

Little, T.A., Prior, D.J., Toy, V.G., 2016. Are quartz LPOs predictably oriented with respect to the shear zone boundary?: a test from the Alpine Fault mylonites, New Zealand. G-cubed 17, 981–999.

Marques, F.O., Coelho, S., 2003. 2-D shape preferred orientations of rigid particles in transtensional viscous flow. J. Struct. Geol. 25, 841–854.

Means, W.D., 1989. Stretching faults. Geology 17, 893–896.

Montagnat, M., Castelnau, O., Bons, P.D., Faria, S.H., Gagliardini, O., Gillet-Chaulet, F., Grennerat, F., Griera, A., Lebensohn, R.A., Moulinec, H., Roessiger, J., Suquet, P., 2014. Multiscale modeling of ice deformation behavior. J. Struct. Geol. 61, 78–108.

Mulchrone, K.F., 2007. Modelling flanking structures using deformable high axial ratio ellipses: insights into finite geometries. J. Struct. Geol. 29, 1216–1228.

Nye, J.F., 1951. The flow of glaciers and ice-sheets as a problem in plasticity. Proc. Roy. Soc. Lond. 207 (1091), 554–572.

Nye, J.F., 1952. The mechanics of glacier flow. J. Glaciol. 2 (12), 82–93.

Passchier, C.W., 1997. The fabric attractor. J. Struct. Geol. 19, 113–127.

Passchier, C.W., 2001. Flanking structures. J. Struct. Geol. 23, 951–962.

Passchier, C.W., Trouw, R.A.J., Goscombe, B., Gray, D., Kröner, A., 2007. Intrusion mechanisms in a turbidite sequence: the Voetspoor and Doros plutons in NW Namibia. J. Struct. Geol. 29, 481–496.

Passchier, C., Heesakkers, V., Coelho, S., 2008. Two mechanisms for forming flanking folds. In: De Paor, D.G. (Ed.), Making Sense of Shear (In Honour of Carol Simpson). Journal of the Virtual Explorer, Electronic Edition. https://doi.org/10.3809/jvirtex.2009.00209.

Peacock, D., Sanderson, D., 1995. Pull-aparts, shear fractures and pressure solution. Tectonophysics 241, 1–13.

Ragan, D.M., 1969. Structures at the base of an ice fall. J. Geol. 77 (6), 647–667.

Ramberg, H., 1975. Particle paths, displacement and progressive strain applicable to rocks. Tectonophysics 28, 1–37.

Ramsay, J.G., Huber, M.I., 1983. The Techniques of Modern Structural Geology. Volume 1: Strain Analysis. Academic Press Inc. Ltd., London.

Robin, P.-Y.F., Cruden, A.R., 1994. Strain and vorticity patterns in ideally ductile transpression zones. J. Struct. Geol. 16, 447–466.

Sanderson, D.J., Marchini, W.R.D., 1984. Transpression. J. Struct. Geol. 6, 449–458.

Sarkarinejad, K., Faghih, A., Grasemann, B., 2008. Transpressional deformations within the Sanandaj-Sirjan metamorphic belt (Zagros Mountains, Iran). J. Struct. Geol. 30, 818–826.

Schwarzacher, W., Untersteiner, N., 1953. Zum Problem der Bänderung des Gletschereises. Sitzungsberichte, Österreichische Akademie der Wissenschaften, Mathematisch-naturwissenschaftliche Klasse. Abteilung IIa 162, 111–145.

Sengupta, S., Ghosh, S.K., 2004. Analysis of transpressional deformation from geometrical evolution of mesoscopic structures from Phulad shear zone, Rajasthan, India. J. Struct. Geol. 26, 1961–1976.

Sharp, M.J., Lawson, W., Anderson, R.S., 1988. Tectonic processes in a surge-type glacier. J. Struct. Geol. 10 (5), 499–515.

Simpson, C., De Paor, D.G., 1993. Strain and kinematic analysis in general shear zones. J. Struct. Geol. 15, 1–20.

Sölva, H., Grasemann, B., Thoni, M., Thiede, R., Habler, G., 2005. The Schneeberg normal fault zone: normal faulting associated with cretaceous SE-directed extrusion in the Eastern Alps (Italy/Austria). Tectonophysics 401, 143.

Sullivan, W.A., Law, R.D., 2007. Deformation path partitioning within the transpressional White Mountain shear zone, California and Nevada. J. Struct. Geol. 29, 583–599.

Talbot, C.J., Sokoutis, D., 1995. Strain ellipsoids from incompetent dykes: application to volume loss during mylonitization in the Singö gneiss zone, central Sweden. J. Struct. Geol. 17, 927–948.

Tikoff, B., Fossen, H., 1993. Simultaneous pure and simple shear: the unifying deformation matrix. Tectonophysics 217, 267–283.

Tikoff, B., Green, D., 1997. Stretching lineations in transpressional shear zones: an example from the Sierra Nevada Batholith, California. J. Struct. Geol. 19, 29–39.

Untersteiner, N., 1955. Some observations on the banding of glacier ice. J. Glaciol. 2, 502–506.

Waldron, J.W.F., 2005. Extensional fault arrays in strike-slip and transtension. J. Struct. Geol. 27, 23–34.

Wernicke, B., 1981. Low-angle normal faults in the Basin and Range Province-Nappe tectonics in an extending orogen. Nature 291, 645–648.

Whitney, D.L., Teyssier, C., Heizler, M.T., 2007. Gneiss domes, metamorphic core complexes, and wrench zones: thermal and structural evolution of the Nigde Massif, central Anatolia. Tectonics 26, TC5002. https://doi.org/10.1029/2006TC002040.

Wiesmayr, G., Grasemann, B., 2005. Sense and non-sense of shear in flanking structures with layer-parallel shortening: implications for fault-related folds. J. Struct. Geol. 27, 249–264.

Wilson, C.J.L., Russell-Head, D.S., 1979. Experimental folding in ice and the resultant c-axis fabrics. Nature 279, 49–51.

Xypolias, P., 2010. Vorticity analysis in shear zones: a review of methods and applications. J. Struct. Geol. 32, 2072–2092.

Xypolias, P., Kokkalas, S., Skourlis, K., 2003. Upward extrusion and subsequent transpression as a possible mechanism for the exhumation of HP/LT rocks in Evia Island (Aegean Sea, Greece). J. Geodyn. 35, 303–332.

Xypolias, P., Gerogiannis, N., Chatzaras, V., Papapavlou, K., Kruckenberg, S.C., Aravadinou, E., Michels, Z., 2018. Using incremental elongation and shearing to unravel the kinematics of a complex transpressional zone. J. Struct. Geol. 115, 64–81.

Zuo, Z., Oerlemans, J., 1997. Numerical modelling of the historic front variation and the future behaviour of the Pasterze glacier, Austria. Ann. Glaciol. 24, 234–241.